Nonlinear model reduction to random spectral submanifolds in random vibrations

Xu, Zhenwei; Kaundinya, Roshan S.; Jain, Shobhit; Haller, George

DOI
10.1016/j.jsv.2024.118923

Publication date
2025

Document Version
Final published version

Published in
Journal of Sound and Vibration

Journal of Sound and Vibration 600 (2025) 118923

Contents lists available at ScienceDirect

Journal of Sound and Vibration

journal homepage: www.elsevier.com/locate/jsvi

Nonlinear model reduction to random spectral submanifolds in random vibrations

Zhenwei Xu [a], Roshan S. Kaundinya [a], Shobhit Jain [b], George Haller [a,*]

[a] Institute for Mechanical Systems, ETH Zürich, Switzerland
[b] Delft Institute of Applied Mathematics, TU Delft, Netherlands

ARTICLE INFO

Keywords:
Random vibrations
Invariant manifolds
Reduced-order modeling
Spectral submanifolds

ABSTRACT

Dynamical systems in engineering and physics are often subject to irregular excitations that are best modeled as random. Monte Carlo simulations are routinely performed on such random models to obtain statistics on their long-term response. Such simulations, however, are prohibitively expensive and time consuming for high-dimensional nonlinear systems. Here we propose to decrease this numerical burden significantly by reducing the full system to very low-dimensional, attracting, random invariant manifolds in its phase space and performing the Monte Carlo simulations on that reduced dynamical system. The random spectral submanifolds (SSMs) we construct for this purpose generalize the concept of SSMs from deterministic systems under uniformly bounded random forcing. We illustrate the accuracy and speed of random SSM reduction by computing the SSM-reduced power spectral density of the randomly forced mechanical systems that range from simple oscillator chains to finite-element models of beams and plates.

1. Introduction

Excitation without temporally recurrent features is ubiquitous in nature and hence many mechanical structures are subjected to it. Examples include wind forcing on bridges, turbulent airflow over airplane wings and seismic forces from earthquakes on buildings. This has been stimulating significant interest in stochastic approaches to mechanics problems, dating back to seminal contributions by Caughey [1] and Crandall [2] (see also Crandall and Mark [3], Caughey [4], Wirschin et al. [5] and Li and Chen [6] for surveys).

Notable technical advances in the analysis of stochastically forced systems are perturbative methods for higher-order statistics in weakly nonlinear systems (see, e.g., Caughey [1] and Crandall [2]) and stochastic averaging for systems with weak nonlinearity and weak damping (see Roberts and Spanos [7]). In these and other related methods, random vibrations have been modeled either as random dynamical systems (i.e., ordinary differential equations appended with a white noise perturbation) or stochastic differential equations (i.e., Itô processes for the differential of the unknown with a drift term and a Brownian motion term); see Arnold [8] and Duan [9] for discussions of the technicalities involved in both approaches.

To a large extent, both of these modeling approaches are driven by the convenience of having the Kolmogorov and the Fokker–Planck partial differential equations (PDEs) at one's disposal for the first-order statistics of the response. Both approaches, however, allow for the occurrence of arbitrarily large forcing values with nonzero probability, which is unrealistic in physical settings, as already pointed out by Caughey [4]. A similar situation arises in other fields with prominent randomness, such as financial modeling,

* Corresponding author.
E-mail address: georgehaller@ethz.ch (G. Haller).

https://doi.org/10.1016/j.jsv.2024.118923
Received 9 July 2024; Received in revised form 18 December 2024; Accepted 19 December 2024
Available online 25 December 2024

in which stochastic ODEs with Brownian motion are convenient but do not quite reproduce practically observed financial time series (see, e.g., Ghaoui and Calafiore [10]). Even from a purely mathematical perspective, showing the existence of the random equivalents of deterministic structures (such as invariant manifolds) in the phase space under arbitrarily large perturbations is a futile undertaking. Indeed, even simple structurally stable dynamical features, such as asymptotically stable fixed points or attracting limit cycles, will be destroyed by unbounded perturbations.

For these reasons, we consider here the physically more realistic case of external random forcing whose realizations are uniformly bounded in time. Under this assumption, one may reasonably seek random extensions of dynamical structures that are known to enable mathematically rigorous model reduction in deterministic vibratory systems. Such structures are known in deterministic vibrations since the seminal work of Shaw and Pierre [11] on nonlinear normal modes (NNMs), defined as invariant manifolds tangent to modal subspaces of mechanical systems (see also Kerschen et al. [12], Mikhlin and Avramov [13] and Mikhlin and Avramov [14] for reviews).

More recent work by Haller and Ponsioen [15] and Haller et al. [16] revealed that the envisioned deterministic NNMs only exist under specific nondegeneracy and nonresonance conditions. Even under those conditions, NNMs are never unique. Rather, a continuous family of spectral submanifolds (SSMs) exists that are all tangent to any selected span of nonresonant spectral subspaces. The smoothest such SSM admits a regular Taylor expansion up to the degree of the dynamical system, whereas the remaining secondary (or fractional) SSMs only admit fractional-powered expressions. The general theory of SSMs has also been extended to cover fixed points with instabilities (Haller et al. [16]) and systems subject to uniformly bounded temporally aperiodic forcing, including chaotic forcing (see Haller and Kaundinya [17]).

These results on generalized deterministic SSMs have been implemented in a continually expanding open-source MATLAB code, *SSMTool,* with a growing collection of nonlinear examples (see Jain et al. [18] for the latest version). The package can also handle parametric resonance (see Thurnher et al. [19]) and algebraic constraints (see Li et al. [20]). Matlab- and Python-based open source packages, *SSMLearn* and *fastSSM*, for a purely data-driven extraction of SSMs have also become available (see Cenedese et al. [21] and Axås et al. [22]), broadening the applicability of SSM-based model reduction to diverse fields, such as control of soft robots (see Alora et al. [23]), transition problems in fluids (see Kaszás and Haller [24]) and modeling of fluid–structure interactions from videos (see Xu et al. [25]).

The idea of extending the Shaw–Pierre NNM concept to random vibrations is already implicit in the work of Worden et al. [26]. Motivated by the full decoupling of linear systems in a modal basis, these authors propose an alternative definition of deterministic NNMs as n statistically independent nonlinear mappings from a $2n$-dimensional phase space to two-dimensional (2D) spaces. Worden et al. [26] assume polynomial expansions for these NNM mappings and seek to determine the coefficients in these expansions from the response of the system under stochastic forcing. Specifically, they obtain the polynomial coefficients by minimizing the cross-correlations of envisioned mappings via regression.

Targeting deterministic NNMs via stochastic forcing, Worden et al. [26] implicitly assume that (a) an appropriately modified notion of an invariant manifold continues to exist under stochastic forcing (b) this manifold is in fact the same as the unforced manifold, irrespective of the forcing level. While (a) cannot be guaranteed for the unbounded noise employed in their approach and (b) is generally not the case, the idea is clearly a novel and important step in exploring the fate of NNMs under general forcing and in a data-driven setting. A follow-up paper by Tsialiamanis et al. [27] on the same idea is critical of the first implementation of the idea and uses instead generative adversarial networks to learn the NNM mappings, still under stochastic forcing. More recent work by Simpson et al. [28] explores this idea further by employing long-short term neural networks in the procedure. The dimension of data-driven applications in these advances remains in the tens of degrees of freedom. No explicit reduced-models are obtained in the end, as the approach seeks only the mapping from the data to reduced coordinates and back.

In contrast, SSMLearn has been successfully employed to extract predictive deterministic SSM-reduced models from experimental measurements (see Cenedese et al. [29]), experimental videos of continua (of infinite degrees of freedom, see Cenedese et al. [21] and Yang et al. [30]) and numerical data from finite-element codes exceeding a million degrees of freedom (see Cenedese et al. [31]). For this reason, we do not seek here a further improvement of data-driven deterministic SSM extraction. Rather, we focus on what the above cited statistical approaches implicitly assume: the existence of random SSMs in stochastically forced deterministic systems. We show that a combination of prior results on a class of random invariant manifolds and recent results on deterministic invariant manifolds can be used to infer the existence of random SSMs and their reduced dynamics with full mathematical rigor.

This paper is organized as follows. We first prove the existence of random spectral submanifolds (random SSMs) for randomly forced dynamical systems. These SSMs turn out to exist under smoothness and nonresonance conditions on the deterministic unforced system and under a uniform boundedness assumption on the random forcing. We also derive leading-order formulas for computing reduced models on random SSMs. We then demonstrate the performance of random SSM reduction in four examples: a suspension system also known as a quarter-car model moving on an irregular road, a building model subject to earthquakes, a von Kármán beam undergoing random base excitation and a rectangular von Kármán plate placed in a windy medium. We conclude by summarizing our contributions and discussing future work.

2. SSMs in randomly forced systems

2.1. Setup

We consider small random perturbations of a deterministic set of first-order nonlinear ordinary differential equations (ODEs) with an attracting fixed point. The randomness of the process is introduced via the dependence of the random perturbation on

elements ν of a probability space $\mathcal{V}$, which is endowed with a probability measure $\mathbb{P}$ and a corresponding sigma algebra $\mathcal{F}$. The evolving randomness along trajectories will be induced by a metric dynamical system $\theta^t : \mathcal{V} \to \mathcal{V}$ that creates a time-dependent random variable $\theta^t(\nu)$ on which the random differential equation depends in a smooth and uniformly bounded fashion.

This smooth dependence will guarantee uniform boundedness for the noise in time, which is a realistic assumption for applications in mechanics. In contrast, randomness modeled by classic stochastic differential equations (or Itô processes) can display arbitrarily large changes in the noise over short periods of time. Such unbounded perturbations would be unrealistic in our context of real-life mechanical systems subject to noisy excitation. This was already pointed out in early work on random vibrations by Caughey [4], who observed that unbounded noise is a convenient assumption that is unsupported by physics but yields simpler statistics. We do not suggest that this convenience assumption leads to fundamentally incorrect results; we simply choose not to make it. We refer to Arnold [8] and Duan [9] as general texts on random dynamical systems and stochastic differential equations.

Based on these preliminaries, we consider a random differential equation

$$\dot{\mathbf{x}} = \mathbf{A}\mathbf{x} + \mathbf{f}_0(\mathbf{x}) + \epsilon \mathbf{g}\left(\mathbf{x}, \theta^t(\nu)\right), \quad \mathbf{x} \in D \subset \mathbb{R}^n, \quad 0 \le \epsilon \ll 1, \quad \mathbf{f}_0(\mathbf{x}) = \mathcal{O}\left(|\mathbf{x}|^2\right), \tag{1}$$

on the probability space $(\mathcal{V}, \mathcal{F}, \mathbb{P})$, where $\mathbf{f}_0 : D \subset \mathbb{R}^n \to \mathbb{R}^n$ is of smoothness class $C^r(D)$ with $r \ge 2$. The uniformly bounded function $\mathbf{g}$ is at least of class C^1 in $\mathbf{x} \in D$, C^0 in t for fixed ν, and measurable in ν. The domain D is assumed compact and forward invariant for $\epsilon = 0$. An example of such a random ODE would be a stochastic ODE that depends on a Brownian motion confined by reflecting boundaries. Another practical example would be a non-autonomous ODE whose time dependence is generated on the fly at discrete time instances via a random variable with values in the $[0, 1]$ interval.

2.2. The unforced system ($\epsilon = 0$)

We assume that $\mathbf{x} = 0$ is a stable hyperbolic fixed point for Eq. (1) and the set D lies fully in the domain of attraction of this fixed point. The linearized ODE at the fixed point is then

$$\dot{\mathbf{x}} = \mathbf{A}\mathbf{x}, \tag{2}$$

and the eigenvalues $\{\lambda_j\}_{j=1}^n$ of $\mathbf{A}$ can be ordered so that

$$\mathrm{Re}\lambda_n \le \mathrm{Re}\lambda_{n-1} \le \cdots \le \mathrm{Re}\lambda_1 < 0 \tag{3}$$

holds. We assume, for simplicity, that $\mathbf{A}$ is diagonalizable, in which case there are n real eigenspaces $E_1, E_2, \ldots, E_n$ corresponding to the eigenvalues listed in (3). Each eigenspace corresponding to a real eigenvalue is one-dimensional and those corresponding to a complex conjugated pair are two-dimensional.

We consider a *slow spectral subspace*

$$E = E_1 \oplus \ldots \oplus E_s, \quad \dim E = d, \tag{4}$$

spanned by the first s eigenspaces of $\mathbf{A}$. If all the eigenspaces correspond to single real eigenvalues, then $d = s$. If all the eigenspaces correspond to single complex conjugate pairs, then $d = 2s$. We also define the collection of the remaining eigenspaces of $\mathbf{A}$ as a fast spectral subspace F with dimension $n - d$.

By construction, E is a d-dimensional, attracting invariant subspace of the linearized ODE (2) that is spanned by the d slowest decaying solution families of this ODE. After a possible linear change of coordinates, we may assume that

$$E = \left\{\mathbf{x} \in \mathbb{R}^n : \mathbf{x}_{d+1} = \cdots = \mathbf{x}_n = 0\right\}, \quad \mathbf{A} = \begin{pmatrix} \mathbf{A}_E & 0 \\ 0 & \mathbf{B} \end{pmatrix}, \tag{5}$$

with $\mathbf{A}_E \in \mathbb{R}^{d\times d}$ and $\mathbf{B} \in \mathbb{R}^{(n-d)\times(n-d)}$. Restriction of the full linear ODE to E gives an exact, d-dimensional reduced-order model with which all solutions of (2) synchronize once the fastest $n - d$ solution components of the system have died out. Specifically, in appropriate coordinates

$$\mathbf{x} = (\boldsymbol{\xi}, \boldsymbol{\eta}) \in \mathbb{R}^d \times \mathbb{R}^{(n-d)}$$

that block-diagonalize $\mathbf{A}$, the d-dimensional reduced linear dynamics on E satisfies

$$\dot{\boldsymbol{\xi}} = \mathbf{A}_E \boldsymbol{\xi}, \quad \mathrm{spect}\mathbf{A}_E = \left\{\lambda_1, \ldots, \lambda_d\right\}.$$

An important question is whether such a model reduction procedure could also be justified for the full nonlinear, random ODE (1).

As a first step in answering this question, we define the *spectral quotient* of E as the positive integer

$$\sigma(E) = \left\lfloor \frac{\mathrm{Re}\lambda_n}{\mathrm{Re}\lambda_1} \right\rfloor,$$

with the half brackets referring to the integer part of a positive real number. The slow spectral subspace E is called *nonresonant* whenever the spectrum of the operator $\mathbf{A}_E$ has no low-order resonance relationship with the spectrum of the operator $\mathbf{B}$. More specifically, E is nonresonant if

$$\sum_{j=1}^d m_j \lambda_j \ne \lambda_k, \quad 2 \le \sum_{j=1}^d m_j \le \sigma(E), \quad k > d. \tag{6}$$

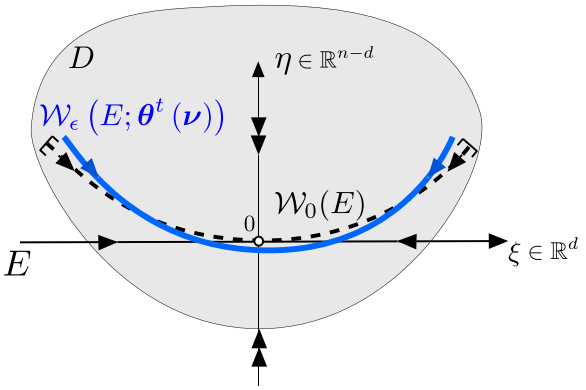

Fig. 1. The geometry of the slow spectral subspace E, the deterministic spectral submanifold $\mathcal{W}_0(E)$ and the random invariant manifold $\mathcal{W}_\epsilon\left(E;\boldsymbol{\theta}^t(\boldsymbol{\nu})\right)$.

Haller and Ponsioen [15] define a *spectral submanifold* $\mathcal{W}_0(E)$ of the deterministic ($\epsilon = 0$) limit of system (1) as the smoothest forward-invariant manifold that is tangent to the spectral subspace E at $x = 0$ and has the same dimension as E. Using results by Cabré et al. [32], Haller and Ponsioen [15] deduce that such a manifold is well-defined and of class C^r as long as $r > \sigma(E)$ and the conditions (3) and (6) are satisfied. In other words, $\mathcal{W}_0(E)$ exists and provides a unique, class C^r, nonlinear continuation of the invariant spectral subspace E in the deterministic limit of the random ODE (1). Near the origin, $\mathcal{W}_0(E)$ can therefore be written as a graph

$$\boldsymbol{\eta} = \mathbf{h}_0(\boldsymbol{\xi}), \tag{7}$$

for some function $\mathbf{h}_0 \in C^r$. With the notation

$$\mathbf{f}_0(\mathbf{x}) = \left(\mathbf{f}_{0\xi}(\boldsymbol{\xi},\boldsymbol{\eta}), \mathbf{f}_{0\boldsymbol{\eta}}(\boldsymbol{\xi},\boldsymbol{\eta})\right),$$

the reduced dynamics on $\mathcal{W}_0(E)$ satisfies the reduced ODE

$$\dot{\boldsymbol{\xi}} = \mathbf{f}_{0\xi}\left(\boldsymbol{\xi}, \mathbf{h}_0(\boldsymbol{\xi})\right), \tag{8}$$

which is an exact reduced-order model for system (1) for $\epsilon = 0$ in a neighborhood of the origin. We show the geometry of the subspace E and the deterministic spectral submanifold $\mathcal{W}_0(E)$ in Fig. 1.

Of interest to us here is the continuation of $\mathcal{W}_0(E)$ and its reduced dynamics for $\epsilon > 0$ in the full random ODE (1). To this end, we define the *spectral gap* $\rho(E)$ associated with E as the integer part of the ratio of the slowest decay rate outside E to the fastest decay rate inside E:

$$\rho(E) = \left\lfloor \frac{\operatorname{Re}\lambda_{d+1}}{\operatorname{Re}\lambda_d} \right\rfloor. \tag{9}$$

Note that $1 < \rho(E) \le \sigma(E)$ by definition. If needed, we reduce the size of the domain D to make sure that all trajectories in $\mathcal{W}(E)$ converge to the fixed point at the origin. In that case, SSM-normal compression rates along each trajectory in $\mathcal{W}(E)$ will be at least $\rho(E)$-times stronger than the SSM-tangential compression rates as $t \to \infty$. In other words, $W(E)$ is a $\rho(E)$-normally hyperbolic invariant manifold by the classic definition of Fenichel [33]. After possibly modifying the boundary of $\mathcal{W}(E)$, we can also assume that $\mathcal{W}(E)$ is an inflowing invariant manifold, i.e., all nonzero trajectories cross the boundary of $\mathcal{W}(E)$ strictly inwards.

2.3. The forced system ($\epsilon > 0$)

With the help of the noise model $\boldsymbol{\theta}^t$ on the probability space $\mathcal{V}$ (see Eq. (1)), the solution operator

$$\mathbf{F}_\epsilon^t : X \times \mathcal{V} \to X, \qquad t \in \mathbb{R}, \tag{10}$$

of the random ODE (1) defines a *random dynamical system* (or *random flow map*) $\mathbf{F}_\epsilon^t : D \to \mathbb{R}^n$ that is measurable in t and over $\mathcal{V} \times X$, and satisfies the *cocycle condition*

$$\begin{aligned} &\mathbf{F}_\epsilon^0(\mathbf{x};\boldsymbol{\nu}) = \mathbf{x}, \\ &\mathbf{F}_\epsilon^{t+s}(\mathbf{x};\boldsymbol{\nu}) = \mathbf{F}_\epsilon^s\left(\mathbf{F}_\epsilon^t(\mathbf{x};\boldsymbol{\nu});\boldsymbol{\theta}^t(\boldsymbol{\nu})\right). \end{aligned} \tag{11}$$

In addition, such a random dynamical system is said to be *class C^r smooth* if the mapping $\mathbf{F}_\epsilon^t(\cdot;\boldsymbol{\nu})$ is of class C^r for all $(t,\boldsymbol{\nu})$.

The second condition in (11) ensures that the evolution along random trajectories satisfies an analogue of the group property of deterministic flows. Specifically, stitching together subsequent segments of a full random trajectory should result in the same final position for the piecewise stitched trajectory and for the full trajectory, even though each segment of the stitched trajectory is initialized under a different element of $\mathcal{V}$ chosen at the start time of the segment. The metric dynamical system $\boldsymbol{\theta}^t$ ensures that

these elements of $\mathcal{V}$ are properly (and deterministically) related to each other along each random trajectory. In modeling the noise in Eq. (1), the probability space $\mathcal{V}$ is commonly selected as the space of continuous paths $\{\nu(s)\}_{s\geq 0}$ with $\nu(0) = 0$. In that case, $\theta^t\nu(\cdot) = \nu(t+\cdot) - \nu(t)$ is called the Wiener shift under which the probability measure $\mathbb{P}$ is invariant and ergodic (see Arnold [8] or Duan [9]).

A *random set* $\mathcal{M}(\nu) \subset D$ is a family of nonempty closed sets such that

$$\nu \mapsto \inf_{\mathbf{y}\in\mathcal{M}(\nu)} \|\mathbf{x}-\mathbf{y}\|$$

is a random variable for any $\mathbf{x} \in D$. Such a random set is a *random manifold* if each $\mathcal{M}(\nu)$ is a manifold. A random manifold is a *random invariant manifold* for the random flow map for system (1) if

$$\mathbf{F}_\epsilon^t\left(\mathcal{M}(\nu);\nu\right) = \mathcal{M}\left(\theta^t(\nu)\right)$$

holds for all $t \in \mathbb{R}$ and $\nu \in \mathcal{V}$. A random manifold $\bar{\mathcal{M}}(\nu) = \mathcal{M}(\nu) \cup \partial\mathcal{M}(\nu)$ with boundary $\partial\mathcal{M}(\nu)$ is called a *random inflowing invariant manifold* (with boundary) if

$$\mathbf{F}_\epsilon^t\left(\mathcal{M}(\nu);\nu\right) \supset \bar{\mathcal{M}}\left(\theta^t(\nu)\right)$$

for all $t < 0$ and all $\nu \in \mathcal{V}$. Similarly, a random manifold $\bar{\mathcal{M}}(\nu)$ is a *random overflowing invariant manifold* (with boundary) if

$$\mathbf{F}_\epsilon^t\left(\mathcal{M}(\nu);\nu\right) \supset \bar{\mathcal{M}}\left(\theta^t(\nu)\right)$$

for all $t > 0$ and all $\nu \in \mathcal{V}$.

In Appendix A, we prove the following main theorem on the existence of random SSMs by combining results of Li et al. [34] and Eldering et al. [35] in our specific setting.

Theorem 1. *Assume that*

$$r \geq \rho(E).$$

Then, for $\epsilon > 0$ small enough:

(i) The random ODE (1) has a class-$C^{\rho(E)}$, random inflowing-invariant manifold $\mathcal{W}_\epsilon(E;\theta^t(\nu))$, which can locally be written as

$$\mathcal{W}_\epsilon(E;\theta^t(\nu)) = \left\{\mathbf{x} = (\xi,\eta) \in D :\ \eta = \mathbf{h}_\epsilon\left(\xi;\theta^t(\nu)\right) = \mathbf{h}_0(\xi) + \epsilon\mathbf{h}_1\left(\xi;\theta^t(\nu),\epsilon\right)\right\},$$

where $\mathbf{h}_1\left(\xi;\theta^t(\nu),\epsilon\right)$ is measurable in ν, and $C^{\rho(E)}$ smooth in ξ and ϵ. Therefore, $\mathcal{W}_\epsilon\left(E;\theta^t(\nu)\right)$ is $\mathcal{O}(\epsilon)$ C^1-close to $\mathcal{W}(E)$ in D.

(ii) $\mathcal{W}_\epsilon\left(E;\theta^t(\nu)\right)$ is $C^{\rho(E)}$-diffeomorphic to $\mathcal{W}(E)$ inside the domain D for all $\nu \in \mathcal{V}$.

(iii) $\mathcal{W}_\epsilon\left(E;\theta^t(\nu)\right)$ attracts any solutions of (1) starting inside D with probability $\mathbb{P} = 1$.

(iv) $\mathcal{W}_\epsilon(E;\theta^t(\nu))$ can be locally written as

$$\mathcal{W}_\epsilon(E;\theta^t(\nu)) = \left\{\mathbf{x} = (\xi,\eta) \in D :\ \eta = \mathbf{h}_\epsilon(\xi;\theta^t(\nu)) = \mathbf{h}_0(\xi) + \epsilon\mathbf{h}_1\left(\xi;\theta^t(\nu),\epsilon\right)\right\}.$$

(v) The dynamics restricted to $\mathcal{W}_\epsilon(E;\theta^t(\nu))$ satisfies the reduced random ODE

$$\begin{aligned}\dot{\xi} &= \mathbf{f}_{0\xi}\left(\xi,\mathbf{h}_\epsilon\left(\xi;\theta^t(\nu)\right)\right) + \epsilon\mathbf{g}_\xi\left(\xi,\mathbf{h}_\epsilon\left(\xi;\theta^t(\nu)\right),\theta^t(\nu)\right)\\ &= \mathbf{f}_{0\xi}\left(\xi,\mathbf{h}_0(\xi)\right) + \epsilon\left[D_\eta\mathbf{f}_{0\xi}\left(\xi,\mathbf{h}_0(\xi)\right)\mathbf{h}_1\left(\xi;\theta^t(\nu),0\right) + \mathbf{g}_\xi\left(\xi,\mathbf{h}_0(\xi),\theta^t(\nu)\right)\right] + \mathcal{O}\left(\epsilon^2\right).\end{aligned} \tag{12}$$

Proof. See Appendix A. □

We show schematically the random inflowing-invariant manifold $\mathcal{W}_\epsilon(E;\theta^t(\nu))$ for one particular $\nu \in \mathcal{V}$ in Fig. 1. By definition, as any random invariant manifold, $\mathcal{W}_\epsilon(E;\theta^t(\nu))$ is time-dependent in any realization of the random ODE (1) and satisfies

$$\mathbf{F}_\epsilon^t\left(\mathcal{W}_\epsilon(E;\nu);\nu\right) \supset \mathcal{W}_\epsilon\left(E;\theta^t(\nu)\right)$$

for all $t \geq 0$.

By statement (iv) of Theorem 1, model reduction to the persisting random invariant manifold $\mathcal{W}_\epsilon\left(E;\theta^t(\nu)\right)$ proceeds along the same lines as in the deterministic case, allowing one to reduce high-dimensional Monte-Carlo simulations to low-dimensional ones. Note that only $\rho(E)$ continuous derivatives can be guaranteed for the random SSM even though its deterministic limit $\mathcal{W}_0(E)$ is of the generally higher smoothness class C^r.

Remark 1 (*Computing the SSM-reduced model*)**.** The graph (7) of the unforced, deterministic SSM and can be calculated to a high degree of accuracy using existing the MATLAB software *SSMTool* (see Jain and Haller [36] and Jain et al. [18]). Therefore, the leading-order reduced-order model (12) on the random SSM $\mathcal{W}_\epsilon\left(E;\theta^t(\nu)\right)$ can be simulated by using $\mathbf{h}_0$ obtained from SSMTool. Note that the block-diagonalization used in Eq. (5) for mathematical exposition is not carried out in SSMTool. Rather, the computations are done directly in the coordinates $\mathbf{x}$ appearing in the random ODE (1).

Remark 2 (*State-independent random forcing*)**.** In applications, the random forcing model frequently has no dependence on the phase space variable $\mathbf{x}$. In that case, we have $\mathbf{g}_\xi\left(\xi,\mathbf{h}_0(\xi),\theta^t(\nu)\right)\equiv\mathbf{g}_\xi\left(\theta^t(\nu)\right)$ and the contributions from terms appearing at $O(\epsilon|\xi|)$ from $\mathbf{D}_\eta\mathbf{f}_{0\xi}\mathbf{h}_1\left(\xi;\theta^t(\nu),0\right)$ in the reduced Eq. (12) can be neglected near the origin compared to $\mathbf{g}_\xi\left(\theta^t(\nu)\right)$. Therefore, we can simply add the projection of the full random forcing on the spectral subspace E to the unforced reduced dynamics in $\mathcal{W}_0(E)$ to obtain the reduced random dynamical system

$$\dot{\xi}=\mathbf{f}_{0\xi}\left(\xi,\mathbf{h}_0(\xi)\right)+\epsilon\mathbf{g}_\xi\left(\theta^t(\nu)\right)+\mathcal{O}\left(\epsilon^2\right). \tag{13}$$

This approximation has been successfully used to predict accurate deterministic forced response in equation- and data-driven examples (see Jain and Haller [36] and Cenedese et al. [21]).

Remark 3 (*Relation to the case of non-Random, aperiodic forcing*)**.** On a single realization of the uniformly bounded random forcing, the forcing becomes deterministic but still aperiodic. Haller and Kaundinya [17] gives asymptotic formulas for the corresponding deterministic, perturbed SSM $\mathcal{W}_\epsilon(E,t)$ up to any finite order of accuracy. The leading order formulas for the SSM-reduced model from Haller and Kaundinya [17] differ from Eq. (12), as we do not anchor the SSM to a unique asymptotic generalized steady state (see Appendix A for details). Furthermore, on each such realization, the SSM is only guaranteed to exist up to a maximal ϵ value that depends on the realization. There is no guarantee that a common, non-zero, maximal ϵ can be chosen for all realizations, which has necessitated the development of random SSM theory described in this paper.

Remark 4 (*Smoothness of the random SSM*)**.** For simplicity, we have considered the domain D small enough so that $\mathcal{W}_0(E)$ had very simple dynamics: all solutions in the deterministic SSM converged to the origin. This enables us to establish that the strength of normal hyperbolicity (i.e., how many times normal attraction overpowers tangential compression along $\mathcal{W}_0(E)$) is precisely the spectral gap $\rho(E)$ defined in Eq. (9), which can be computed purely from the spectrum of the matrix $\mathbf{A}$. This, in turn, enables us to conclude that the random invariant manifold $\mathcal{W}_\epsilon\left(E;\theta^t(\nu)\right)$ is $C^{\rho(E)}$ smooth (see the Appendix for details). On larger D domains, however, $\mathcal{W}_0(E)$ may have nontrivial internal dynamics, i.e., may contain further limit sets in addition to the fixed point at $\mathbf{x}=0$. In that case, an analog of Theorem 1 continues to hold as long as $\mathcal{W}_0(E)$ remains normally hyperbolic, i.e., normal attraction rates to $\mathcal{W}_0(E)$ still overpower tangential compression rates everywhere along $\mathcal{W}_0(E)$ as $t\to\infty$. Establishing the strength of normal hyperbolicity of $\mathcal{W}_0(E)$ in that case, however, requires the exact knowledge of the asymptotic ratio of normal and tangential compression rates along all limit sets within $\mathcal{W}(E)$. This strength (and hence the guaranteed smoothness) of the persisting $\mathcal{W}_\epsilon\left(E;\theta^t(\nu)\right)$ will then be the integer part of the minimum of these ratios taken over all limit sets of $\mathcal{W}_0(E)$.

Remark 5 (*Existence of random SSMs for repelling fixed points*)**.** Results similar to those listed in Theorem 1 hold when the origin is a repelling fixed point, i.e., the matrix A has eigenvalues

$$\mathrm{Re}\lambda_n\geq\mathrm{Re}\lambda_{n-1}\geq\cdots\geq\mathrm{Re}\lambda_1>0. \tag{14}$$

In that case, the surviving random invariant manifold $\mathcal{M}_\epsilon(\theta^t(\nu))$ is overflowing and repels all initial conditions in D for small enough $\epsilon>0$.

Remark 6 (*Leading order parametrization correction to the random SSM*)**.** If we further assume $\mathbf{h}_1(\xi;\theta^t(\nu),0)$ to be C^1 in time, then one can express the leading-order SSM parametrization $\mathbf{h}_1(\mathbf{0};\theta^t(\nu),0)$ in the form

$$\mathbf{h}_1(\mathbf{0};\theta^t(\nu),0)=((\mathbf{V}_F)_L)^{\mathrm{T}}\int_{-\infty}^{t}e^{\mathbf{A}(t-s)}\left(\mathbb{I}_n-\mathbf{P}_E\right)\mathbf{g}(\mathbf{0},\theta^s(\nu))ds, \tag{15}$$

as we show in Appendix B. Here $\mathbf{P}_E$ is the spectral projection onto the slow subspace E and the columns of $(\mathbf{V}_F)_L\in\mathbb{R}^{n\times(n-d)}$ contain $(n-d)$ left eigenvectors of $\mathbf{A}$ spanning the fast subspace F.

3. Examples

We consider mechanical systems of the form

$$\mathbf{M}\ddot{\mathbf{q}}+\mathbf{C}\dot{\mathbf{q}}+\mathbf{K}\mathbf{q}+\mathbf{f}_{nl}(\mathbf{q},\dot{\mathbf{q}})=\mathbf{p}\left(\theta^t(\nu),\mathbf{q},\dot{\mathbf{q}}\right), \tag{16}$$

where $\mathbf{M},\mathbf{C},\mathbf{K}\in\mathbb{R}^{n\times n}$ are positive definite mass matrix, and the positive semidefinite damping and stiffness matrices, respectively; $\mathbf{q}\in\mathbb{R}^n$ is the vector of generalized coordinates; the function $\mathbf{f}_{nl}(\mathbf{q},\dot{\mathbf{q}})$ is a vector of geometric and material nonlinearities; and $\mathbf{p}\left(\theta^t(\nu),\mathbf{q},\dot{\mathbf{q}}\right)$ is a uniformly bounded external or parametric forcing vector with random time dependence.

The second order system (16) can be rewritten in its first order system form

$$\dot{\mathbf{x}}=\mathbf{A}\mathbf{x}+\mathbf{f}_0(\mathbf{x})+\mathbf{g}(\theta^t(\nu),\mathbf{x}),\quad \mathbf{x}=(\mathbf{q},\dot{\mathbf{q}})^{\mathrm{T}}, \tag{17}$$

where

$$\mathbf{A}=\begin{bmatrix}\mathbf{0} & \mathbf{I}\\ -\mathbf{M}^{-1}\mathbf{K} & -\mathbf{M}^{-1}\mathbf{C}\end{bmatrix},\quad \mathbf{f}_0(\mathbf{x})=\begin{bmatrix}\mathbf{0}\\ -\mathbf{M}^{-1}\mathbf{f}_{nl}(\mathbf{q},\dot{\mathbf{q}})\end{bmatrix},$$

$$\text{and} \quad \mathbf{g}(\theta^t(\nu), \mathbf{x}) = \begin{bmatrix} \mathbf{0} \\ \mathbf{M}^{-1}\mathbf{p}\left(\theta^t(\nu), \mathbf{q}, \dot{\mathbf{q}}\right) \end{bmatrix}.$$

In all our examples, the unforced system admits an asymptotically stable fixed point at $\mathbf{x} = 0$. We will assume that a uniform bound on the forcing is defined as

$$\epsilon = \limsup_{t\in\mathbb{R}, \nu\in\mathcal{V}, \mathbf{x}\in D} \left|\mathbf{g}(\theta^t(\nu), \mathbf{x})\right|$$

for $D \subset \mathbb{R}^{2n}$, i.e., we subsume the book-keeping parameter ϵ appearing in Eq. (1) into the definition of the forcing for convenience.

Random force generation

In our examples, the forcing vector $\mathbf{p}\left(\theta^t(\nu), \mathbf{q}, \dot{\mathbf{q}}\right)$, will have the form $\epsilon\theta^t(\nu)(\mathbf{v}+\mathbf{f}_\mathbf{p}(\mathbf{q}, \dot{\mathbf{q}}))$ where $\mathbf{v} \in \mathbb{R}^n$ is a constant vector, $\mathbf{f}_\mathbf{p} \in \mathbb{R}^n$ is a function representing parametric excitation, ϵ is a parameter controlling the magnitude of the uniformly bounded forcing, $\theta^t(\nu)$ is a time-dependent scalar random variable appearing in Eq. (1) that is uniformly bounded in time for any ν. We list three possible ways to generate such noise:

- **Method 1: Force generation from a spectral density.** In some examples the random forcing signal $\theta^t(\nu)$ can be inferred from an empirical spectral density $\boldsymbol{\Phi}_\nu(\omega) = \mathbb{E}[(\theta^\omega(\nu))^2]$. Here $\mathbb{E}$ is the expectation value operator and $\theta^\omega(\nu)$ is the Fourier transform of one realization of the random forcing signal $\theta^t(\nu)$. Following textbook methods (see Preumont [37]), we can numerically evaluate a realization of a forcing signal $\theta^t(\nu)$ from the spectral density $\boldsymbol{\Phi}_\nu(\omega)$. We specify a frequency range $\omega \in [\omega_0, \omega_M]$ which is equally spaced with spacing $\Delta\omega$. The forcing signal for one realization in this frequency window can then be written as

$$\theta^t(\nu) = \sum_{i=0}^{M} \sqrt{2\boldsymbol{\Phi}_\nu(\omega_0 + i\Delta\omega)\Delta\omega}\cos((\omega_0 + i\Delta\omega)t + \phi_i), \tag{18}$$

  where $\omega_N = \omega_0 + M\Delta\omega$ and ϕ_i is a uniform random number from the interval $[0, 2\pi]$. From a numerical perspective, Eq. (18) represents a fast Fourier transform of the spectral density. Note that for every realization, one can regard this signal to lie on a $N-$ dimensional torus, thus the process is only quasi-random.
- **Method 2: Lévy process with a bounded random number generator.** A classic method to generate a truly random process in time is to advect a random ODE describing Brownian motion. However in that case, the random process is an Itô process and the noise generation is sampled from a Gaussian distribution $\mathcal{N}$ which is unbounded. This translates to the increments of the random variable given by $(\theta^{t+\Delta t}(\nu) - \theta^t(\nu))$ following the probability density function $\mathcal{N}(0, \Delta t)$ for all $t \geq 0$. We make this process bounded by prescribing the increments to follow a truncated Gaussian distribution $\mathcal{NT}(0, \Delta t; a, b)$, where the density function is 0 outside the amplitude interval $[a, b]$. If we choose a symmetric interval and also ensure the interval encompasses regions of high probability, the truncated Gaussian increments offers a bounded Brownian motion which is very close to the one generated by an Itô process. Since all our examples are mechanical systems, it is convenient to model the randomness using a second-order system (see Kozin [38]) of the form

$$m\ddot{a} + c\dot{a} + ka = \theta^t(\nu), \tag{19}$$

  where ä, $\dot{a}$ or a are interpreted as physically relevant scalar quantities like ground acceleration during an earthquake, uniform fluid velocity or road elevation. The forcing $\theta^t(\nu)$ is a random process generated from a truncated Gaussian distribution. This setup offers practical benefits when implemented in a numerical scheme as one can evaluate the random forced response in real time by coupling the above ODE to the mechanical system (16).
- **Method 3: Itô process with reflective boundary conditions.** Another possible method to implement a bounded noise generator is to impose doubly reflective boundary conditions on one of the stochastic random variables generated from Eq. (19) using a Gaussian noise model for $\theta^t(\nu)$. The generated random variable will always be confined to $[-1, 1]$.

Random forced response evaluation

In our examples, the linear part of the unforced mechanical system has a slow spectral subspace E with $d = 2$ (see Eq. (4)). Therefore, under uniformly bounded random forcing, Theorem 1 is applicable. This allows us to construct a 2D time-dependent random SSM $\mathcal{W}_\epsilon\left(E; \theta^t(\nu)\right)$. Specifically, we use *SSMtool* by Jain et al. [18] to compute the autonomous SSM $\mathcal{W}_0(E)$ as a graph $\boldsymbol{\eta} = \mathbf{h}_0(\boldsymbol{\xi})$ and its reduced dynamics $\mathbf{f}_{\boldsymbol{\xi}}(\boldsymbol{\xi}, \mathbf{h}_0(\boldsymbol{\xi}))$ as order-N multivariate polynomials. We then explicitly compute the leading-order corrections (listed in Theorem 1) to obtain the random SSM-reduced model.

We test the accuracy of the random reduced-order models obtained in this fashion by performing Monte Carlo simulations. We repeatedly sample m random forcing realizations using one of the outlined methods (see Methods 1–3) and record the random forced response outcomes of the full and reduced-order models for every realization. We further compute the averaged spectral density (PSD) matrix $\boldsymbol{\Phi}_\mathbf{x}(\omega) \in \mathbb{C}^{2n\times 2n}$ defined as (see Papoulis [39])

$$\boldsymbol{\Phi}_\mathbf{x}(\omega) = \mathbb{E}[\mathbf{x}(\omega)(\mathbf{x}(\omega))^\dagger] = \frac{1}{m}\sum_{j=1}^{m} \mathbf{x}^j(\omega)(\mathbf{x}^j(\omega))^\dagger, \tag{20}$$

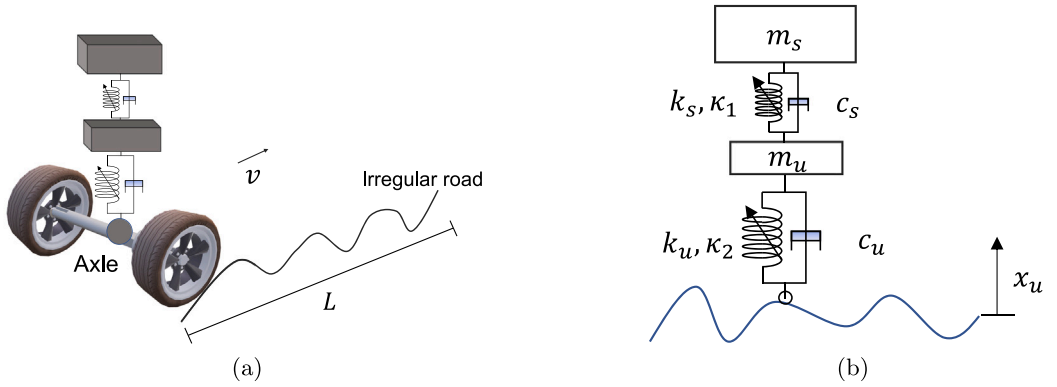

Fig. 2. Left: An illustration of the suspension model of Gobbi and Mastinu [43] moving with speed v along an irregular road of length L. Right: A side profile of the model with system parameters shown.

where $\mathbf{x}^j(\omega)$ is the fast-Fourier transform of the forced outcome $\mathbf{x}^j(t)$ and $[\cdot]^\dagger$ denotes the complex conjugate transpose operation. Note that the diagonal entries of $\boldsymbol{\Phi}_{\mathbf{x}}(\omega)$ are real and represent the energy content of our outcomes. We will plot one of these diagonal entries against the frequency ω to visualize the performance of the reduced-order model in comparison to the full system.

We label a diagonal entry of the matrix as $\phi^f_{\mathbf{x}}(\omega)$, where f refers to a specific position or velocity component of the system. For time integration, we use implicit methods for the full system (see Geradin and Rixen [40]). For the full system simulation in Method 1, we use the implicit Newmark scheme. In Methods 2 and 3, we formulate a second-order implicit scheme provided in Burrage et al. [41]. For the time integration of SSM-reduced systems, we apply a Runge–Kutta scheme as described in Kloeden and Platen [42]. We also advect both the full and the SSM-reduced models from the same initial condition, which always lies on the random SSM.

3.1. Suspension system moving on an irregular road

For the design of the suspension of a car or an offshore platform, one needs to model the stability of these systems under road or sea irregularity. We use here a simplified model of such a suspension proposed by Gobbi and Mastinu [43], as shown in Fig. 2. We modify the original example by allowing the springs to have nonlinear cubic stiffness to model additional hardening or softening behaviors of the spring material. This nonlinearity coupled with the irregular road leads to a parametric forcing experienced by the suspension system.

The equations of motion (16), with $\mathbf{q} = (x_s, x_u)^\mathsf{T}$ denoting the displacements of the spring blocks in the suspension system, are specifically

$$\mathbf{M} = \begin{bmatrix} m_s & 0 \\ 0 & m_u \end{bmatrix}, \quad \mathbf{C} = \begin{bmatrix} c_s & -c_s \\ -c_s & c_s + c_u \end{bmatrix}, \quad \mathbf{K} = \begin{bmatrix} k_s & -k_s \\ -k_s & k_s + k_u \end{bmatrix}, \tag{21}$$
$$\text{and } \mathbf{f}_{nl}(\mathbf{q}) = \begin{pmatrix} \kappa_1(x_s - x_u)^3 \\ -\kappa_1(x_s - x_u)^3 + \kappa_2 x_u^3 \end{pmatrix}.$$

In Eq. (21), we have ignored gravity for simplicity, which will slightly perturb the equilibrium configuration from $\mathbf{x} = \mathbf{0}$. We further assume that the system is traveling at a constant speed v along a road of length L. This allows us to write the force exerted by the irregular road on the system as

$$\mathbf{p}\left(\theta^t(v), \mathbf{q}, \dot{\mathbf{q}}\right) = \epsilon \begin{pmatrix} 0 \\ k_u\theta^t(h) + c_u\theta^t(\nabla h)v + \kappa_2[\theta^t(h)]^3 - 3\kappa_2[\theta^t(h)]^2 x_u + 3\kappa_2 x_u^2\theta^t(h) \end{pmatrix}, \tag{22}$$

where h and ∇h are random variables denoting road elevation and gradient, and ϵ is a measure of the overall magnitude of forcing. There are empirical expressions for the spectral densities to model road elevation (see Gobbi and Mastinu [43]) given by

$$\phi_h(\omega) = \frac{A_v b v}{(bv)^2 + \omega^2}, \tag{23}$$

where the coefficients A_v and b depend on the road irregularity, and v is the speed of the system as mentioned.

We estimate the spectral density of the gradient from the elevation as $\phi_{\nabla h}(\omega) = \frac{\omega^2}{v}\phi_h(\omega)$. We then use Method 1 to sample for the stochastic signals $\theta^t(h)$ and $\theta^t(\nabla h)$ until the car completes the travel time $\frac{L}{v}$ on the road. We perform the sampling for 50 forcing realizations ($m = 50$). We set the system parameters as $m_s = 229$ [kg], $m_t = 31$ [kg], $c_s = 120$ [Ns/m], $c_u = 120$ [Ns/m], $k_s = 60$ [kN/m], $k_u = 20$ [kN/m], $\kappa_1 = 250$ [kN/m^3], $\kappa_2 = 30$ [kN/m^3] and $v = 30$ [m/s]. We set the forcing parameters to be $L = 1800$ [m], $A_v = 3.5 \times 10^{-5}$ [m^2] and $b = 0.4$ [rad/m]. The values of road roughness are taken from Gobbi and Mastinu [43].

Fig. 3 shows the power spectral density $\phi^{x_s}_{\mathbf{x}}(\omega)$ of the displacement of the upper mass m_s in decibel [dB], calculated for the linear system, the full nonlinear system and the random SSM-reduced model with an order $N = 7$ multivariate Taylor expansion for two

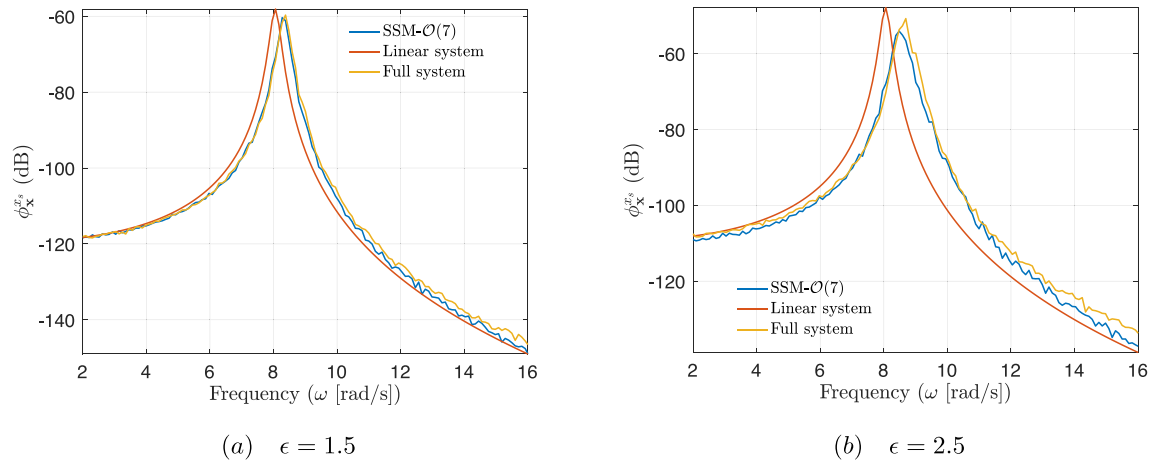

Fig. 3. PSD $\phi_{\mathbf{x}}^{x_s}$ of the displacement of mass m_s obtained from the SSM-reduced order model (blue) and for the full order model simulation (yellow) for two regimes of road irregularities. We also plot in red the analytic PSD for the linear system. (a) $\epsilon = 1.5$ indicates minor road elevations (b) $\epsilon = 2.5$ the road irregularities are amplified. (For interpretation of the references to color in this figure legend, the reader is referred to the web version of this article.)

regimes of road irregularity. When the road irregularity is minimal ($\epsilon = 1.5$), the linear response is close to the nonlinear response of the system, and our random SSM-reduced model reproduces this trend. As expected, once we increase the road irregularity, the nonlinear system deviates from the linear one and our leading-order SSM-reduced model captures this trend. The linear predictions are smooth because we can compute the response statistics analytically (see Appendix B for details).

3.2. Earthquake response of a building

Inspired by building models in civil engineering for modeling earthquake response (see Ho et al. [44]), we now consider a simple n-storey building modeled by a vertical oscillator chain as shown in Fig. 4. Each mass represents a floor and gravity is neglected for simplicity. The system is of the form (16) with

$$\mathbf{q} = [u_1, u_2, \dots u_n]^\top, \quad \mathbf{C} = \beta\mathbf{K} + \alpha\mathbf{M},$$

$$\mathbf{M} = \begin{bmatrix} m_1 & 0 & 0 \\ 0 & \ddots & 0 \\ 0 & 0 & m_n \end{bmatrix} \text{ and } \mathbf{K} = \begin{bmatrix} k_1+k_2 & -k_2 & 0 & \cdots & \cdots \\ -k_2 & k_2+k_3 & -k_3 & 0 & \cdots \\ 0 & -k_3 & k_3+k_4 & \cdots & \cdots \\ \vdots & \vdots & \vdots & \ddots & 0 \\ \vdots & \vdots & \vdots & k_{n-1}+k_n & -k_{n-1} \\ 0 & \cdots & 0 & -k_{n-1} & k_n \end{bmatrix}. \tag{24}$$

The nonlinearity $\mathbf{f}_{nl}(\mathbf{q}, \dot{\mathbf{q}})$ in this example comprises cubic nonlinear springs placed between neighboring storeys with hardening parameter κ. To model earthquake response, we use Method 3 to generate bounded horizontal ground acceleration noise. Specifically, we use the random variable a in Eq. (19) with parameters $k = 2\times10^{-2}$ [N/m], $c = 1\times10^{-1}$ [Ns/m] and $m = 5\times10^{-3}$ [kg]. The forcing vector is $\mathbf{p}\left(\theta^t(\nu)\right) = \epsilon\ddot{u}_G(m_1, \dots, m_n)^\top$, where ϵ is a measure of the ground acceleration intensity and $\ddot{u}_G = a$.

We set the building parameters as $m_1 = m_2 = \cdots = m_n = 7$ [kg], $\alpha = 0$ [Hz], $\beta = 0.0198$ [s], $k_1 = \cdots = k_n = 4555$ [N/m] and $\kappa = 2000$ [N/m^3]. The total number of floors in our building is $n = 10$. Similarly to the previous example, we perform $m = 50$ Monte Carlo simulations and compute the averaged PSD for the degree of freedom u_{10}, which represents the roof of our building model. We find that computing an order $N = 5$ random SSM-reduced model is sufficient to reproduce the statistics of the full system.

In contrast to the suspension model in Section 3.1, the current setup induces truly stochastic forcing in time (see Methods 1–3); is maximally coupled with nonlinear springs; and is of higher dimensions. Our plots in Figs. 5a, b indicate that a 2D random SSM model suffices to capture the PSD of the full system.

Our leading-order random SSM-reduced models capture the deviations from linearity as the forcing magnitude ϵ is increased to 1 (see Fig. 5b). Reduction to the random SSM speeds up the Monte Carlo simulations significantly. In Table 1, we show that the time for the full simulation is nearly 7 times the combined time taken for constructing the SSM-reduced order model and performing the reduced Monte Carlo simulations (just 35 s).

3.3. Random base excitation of a von Kármán beam

Our previous examples focused on discrete models with localized spring nonlinearities. We now proceed to demonstrate the applicability of our methods to more challenging continuum beam models with distributed nonlinearities. We use a finite element

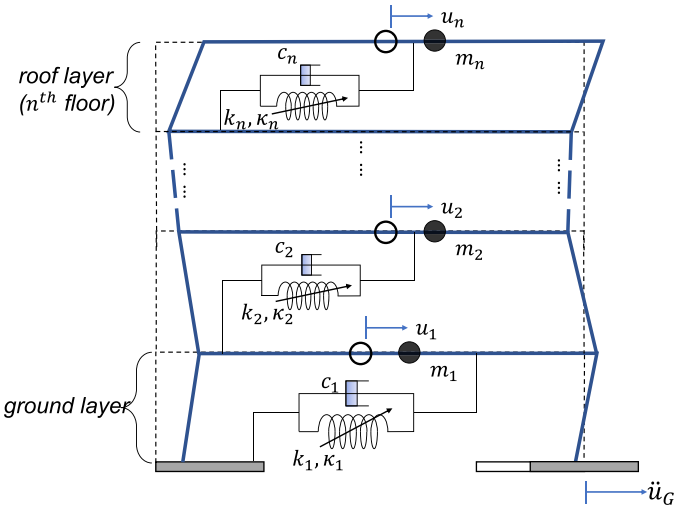

Fig. 4. Schematic model of n-storey building under seismic excitation.

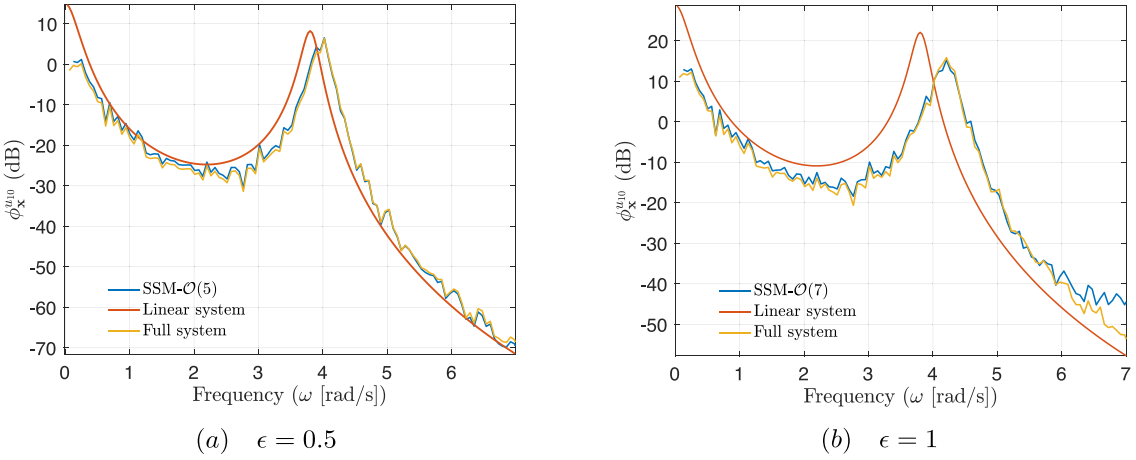

Fig. 5. PSD $\phi_x^{u_{10}}$ of the roof displacement of the building, from the SSM-reduced model (blue) and from the full simulation (yellow) for two earthquake magnitudes. We also plot in red the analytic PSD for the linear system. (a) $\epsilon = 0.5$ models small ground acceleration intensity. (b) $\epsilon = 1$ models large ground acceleration intensity. (For interpretation of the references to color in this figure legend, the reader is referred to the web version of this article.)

Table 1
Run times for the full building model and its random SSM-reduced counterpart for 50 Monte Carlo simulations in the $\epsilon = 1$ forcing regime. All computations were performed on MATLAB version 2022b installed on 50 nodes of the ETH Zürich Euler super-computing cluster with Intel(R) Xeon(R) CPU E3-1284L v4 @ 2.90 GHz processor.

Full system (HH:MM:SS)	2D SSM (HH:MM:SS)	Number of MC simulations
00:03:22	00:00:35	50

model (FEM) approximation for the von Kármán beam as described by Jain et al. [45] which is based on textbook methods by Reddy [46].

Specifically, the FEM is derived from non-dimensional PDEs governing the beam dynamics (see Jain et al. [45]). These PDEs were obtained assuming the Euler–Bernoulli hypothesis for bending and the von Kármán strain approximation allowing for moderate rotations. These assumptions also imply the von Kármán beam model is only accurate for modeling beam displacements that are comparable to the beam thickness. The PDEs are discretized using finite elements, where linear shape functions are used for modeling the axial displacements and cubic shape functions for the remaining degrees of freedom. If we denote with **u** the axial components

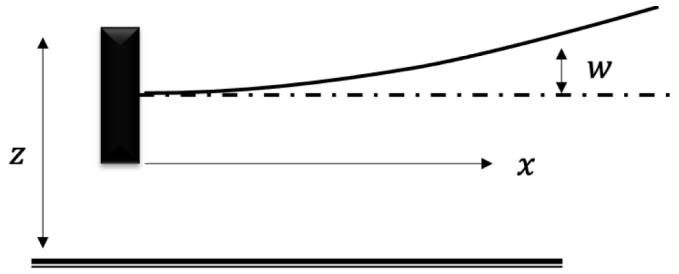

Fig. 6. Schematic view of a cantilevered beam model. The material density is $\rho = 2,700$ [kg/m^3], the Young's modulus is $E = 70$ [GPa], the Poisson's ratio is 0.3, the material viscous damping rate $\kappa = 10^8$ [Pa s], the length is $l = 1$ [m], the width is $w = 1$ [m] and the thickness is $h = 0.001$ [m].

Table 2
Run times for beam model and reduced model for 50 Monte Carlo simulations in the $\epsilon = 1$ forcing regime. All computations were performed on MATLAB version 2022b installed on 50 nodes of the ETH Zürich Euler super-computing cluster with Intel(R) Xeon(R) CPU E3-1284L v4 @ 2.90 GHz processor.

Full system (HH:MM:SS)	2D SSM (HH:MM:SS)	Number of MC simulations
02:39:42	00:01:26	50

and with $\mathbf{v}$ the non-axial displacements, the ODE describing the FEM under time varying axial loads $\mathbf{q}_\mathbf{u}(t)$ and transverse loads $\mathbf{q}_\mathbf{v}(t)$ take the form:

$$\begin{aligned}\mathbf{M}_1\ddot{\mathbf{v}} + \zeta\xi\left(\mathbf{K}_1 + \boldsymbol{C}(\mathbf{v})\right)\dot{\mathbf{v}} + \zeta\boldsymbol{D}(\mathbf{v})\dot{\mathbf{u}} + \mathbf{K}_1\mathbf{v} + \frac{1}{\xi}\boldsymbol{\mathcal{F}}(\mathbf{v},\mathbf{u}) + \boldsymbol{\mathcal{G}}(\mathbf{v}) = \mathbf{q}_\mathbf{v}(t),\\ \mathbf{M}_2\ddot{\mathbf{u}} + \frac{\zeta}{\xi}\mathbf{K}_2\dot{\mathbf{u}} + \zeta\boldsymbol{\mathcal{E}}(\mathbf{v})\dot{\mathbf{v}} + \frac{1}{\xi^2}\mathbf{K}_2\mathbf{u} + \frac{1}{\xi}\boldsymbol{\mathcal{H}}(\mathbf{v}) = \mathbf{q}_\mathbf{u}(t).\end{aligned} \tag{25}$$

Here $\xi = h/l$ is the thickness-to-length ratio, and $\zeta = \frac{\kappa}{l\sqrt{E\rho}}$ is a dimensionless material constant. $\mathbf{M}_1$ and $\mathbf{M}_2$ denote symmetric mass matrices and $\mathbf{K}_1$ and $\mathbf{K}_2$ are symmetric stiffness matrices. The terms $\boldsymbol{\mathcal{F}}(\mathbf{v},\mathbf{u})$, $\boldsymbol{\mathcal{G}}(\mathbf{v})$ and $\boldsymbol{\mathcal{H}}(\mathbf{v})$ denote the nonlinear elastic internal forces, whereas $\boldsymbol{C}(\mathbf{v})$, $\boldsymbol{D}(\mathbf{v})$ and $\boldsymbol{\mathcal{E}}(\mathbf{v})$ are nonlinear viscoelastic damping forces. This model is implemented in a finite-element solver Jain et al. [47], which ultimately yields the matrices $\mathbf{M}$, $\mathbf{C}$, $\mathbf{K}$ and the nonlinearity by $\mathbf{f}_{nl}(\mathbf{q},\dot{\mathbf{q}})$ in the form (16) for specific parameter values and boundary conditions. We use 20 beam elements and impose a cantilevered boundary condition at one end to describe the continuum model, which results in $n = 60$ degrees of freedom. The position vector of the finite element model is $\mathbf{q} = \left(u_1, \quad z_1, \quad w_1, \quad \dots \quad u_{20}, \quad z_{20}, \quad w_{20}\right)^\top$. Here u is the discretized axial displacement, z the discretized transverse displacement and w the discretized deflection angle measured from the beam axis of each finite element. In Fig. 6, we show the beam and list the parameters used in our simulations. These parameter values correspond to a slender sheet made up of aluminum.

We subject this beam to random base excitation, which emulates seismic excitations applied to the cantilevered end of the beam. Accordingly, the forcing vector takes the form $\mathbf{p}\left(\theta^t(\nu)\right) = -\epsilon\theta^t(\nu)\mathbf{M}\left(0, \quad 1, \quad 0, \quad \dots \quad, 0, \quad 1, \quad 0\right)^\top$. To generate the bounded random signal $\theta^t(\nu)$ we use Method 2 and output the random variable ä for parameter values $m = 5$ [kg], $c = 100$ [Ns/m], $k = 20$ [N/m] from (19).

We monitor the transverse tip displacement of the beam for two maximal base accelerations under the forcing parameters $\epsilon = 0.5$ and $\epsilon = 1$. We find that computing an order $N = 7$ random SSM-reduced model suffices to reproduce the statistics of the full order model for both forcing magnitudes.

In Figs. 7a,b, we plot the PSD (in dB) of the tip displacement for $m = 50$ Monte Carlo simulations. Our SSM-reduced computations show close agreement with full order model. For larger forcing magnitudes $\epsilon = 1$, the forced response is amplified for all the models (see Fig. 7b). Due to no nonlinear damping, the linear model overestimates the amplification while the leading-order random SSM-reduced model matches the true response accurately.

In Fig. 8, we present the PSD $\phi_\mathbf{x}^{u_5}$ (in dB) and the time history of the axial displacements u_5 at the quarter length of the beam, corresponding to its, 5th element. For comparison, we also include the response of the axial displacement of the linear system. Since a cantilevered configuration does not exhibit coupling between axial and transverse displacements in the linear regime, the axial displacement remains zero for the linear case. Our random SSM-reduced model is able to capture even the trends in the axial response accurately.

As before in Table 2, we list the run times of $m = 50$ Monte Carlo experiments for the full and reduced models. The beam problem has particularly low damping and to reach any relevant statistics one must simulate the forcing realizations for long times. Still, in just under a minute and a half, our random SSM-reduced order models provide averaged forced outcomes. For comparison, the full order model takes roughly 2 h and 40 min for the MC simulations.

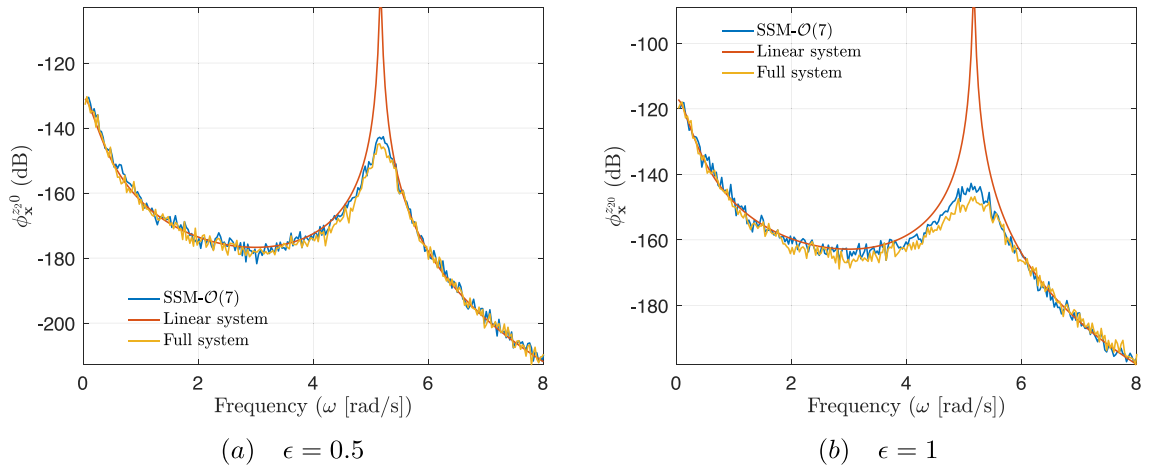

Fig. 7. PSD $\phi_x^{z_{20}}$ of the transverse tip displacement of the beam obtained from the SSM-reduced order model (blue) and from the full order model simulation (yellow) for two earthquake magnitudes. We also plot in red the analytic PSD for the linear system. (a) $\epsilon = 0.5$ models small ground acceleration intensity (b) $\epsilon = 1$ models large ground acceleration intensity. (For interpretation of the references to color in this figure legend, the reader is referred to the web version of this article.)

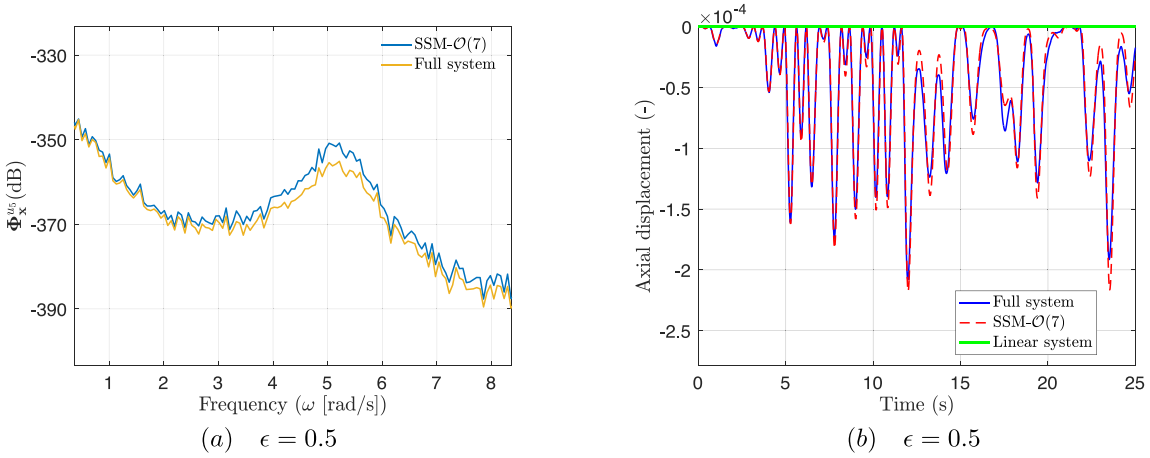

Fig. 8. Axial displacement of the beam at its quarter length obtained from the SSM-reduced order model and full order model simulation for one random forcing realization with forcing magnitude $\epsilon = 0.5$. (a) The PSD $\phi_x^{u_5}$ of the axial displacement. (b) Time series of the axial displacement. The displacement is scaled by the thickness of the beam. (For interpretation of the references to color in this figure legend, the reader is referred to the web version of this article.)

3.4. Von Kármán plate subject to a stochastic pressure field

Our final example is a continuum plate model used in previous SSM-related studies under deterministic forcing (see Jain and Haller [36] and Li et al. [48]). The plate's continuum model is based on similar von Kármán strain approximations as the beam example. These are only valid to describe out-of-plane displacements comparable to the plate's thickness. We modify the plate model to be flat, i.e., set the curvature to zero, and impose simply supported boundary conditions at the edges A and D, as shown in Fig. 9. On these edges, translational displacements are fixed while the rotations are free.

The plate is made up of flat triangular shell elements with each node on the triangle having 6 degrees of freedom. In Fig. 9, we show these elements with the caption stating the parameter values used in our simulations. Specifically, we chose 400 elements which amounts to 1320 degrees of freedom. We plug in these parameter values and element numbers in the FE solver of Jain et al. [47] to obtain the quantities on the left-hand side of Eq. (16).

As for the external forcing, we apply a random uniform body force in the vertical direction $\mathbf{v}$. This models external wind pressure acting on a flat plate, where the wind velocity is the random variable (see Zárate-Miñano et al. [49]). We generate the stochastic velocity using Method 2, with the random variable $\dot{a}$ in Eq. (19) modeling the wind velocity. We set $m = 5$ [kg], $c = 100$ [Ns/m], $k = 20$ [N/m] in Eq. (19) to obtain the realizations for $\dot{a}$. Piecing all this together, the forcing vector is $\mathbf{p}\left(\boldsymbol{\theta}^t(\boldsymbol{\nu})\right) = \epsilon c_d \rho[\dot{a}(t)]^2\mathbf{v}$. We further set $c_d\rho = 2$ [kg/m^3], where c_d is the drag coefficient of the plate in air and ρ is the density of the air.

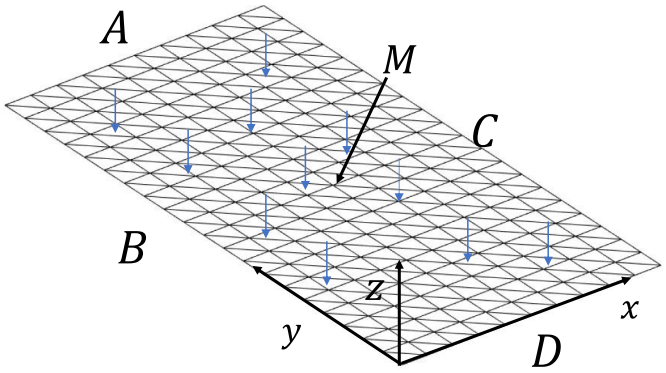

Fig. 9. Schematic view of the von Kármán plate model. The material density is 2700 [kg/m^3], the Young's modulus is 70 [GPa], Poisson's ratio is 0.33, the material viscous damping rate $\kappa = 10^8$ [Pa s], the length is 2 [m], the width is 1 [m] and the thickness 0.01 [m]. Blue arrows indicate the direction of the uniform body force applied. The midpoint of the plate, denoted as M, is used to monitor the output signal. (For interpretation of the references to color in this figure legend, the reader is referred to the web version of this article.)

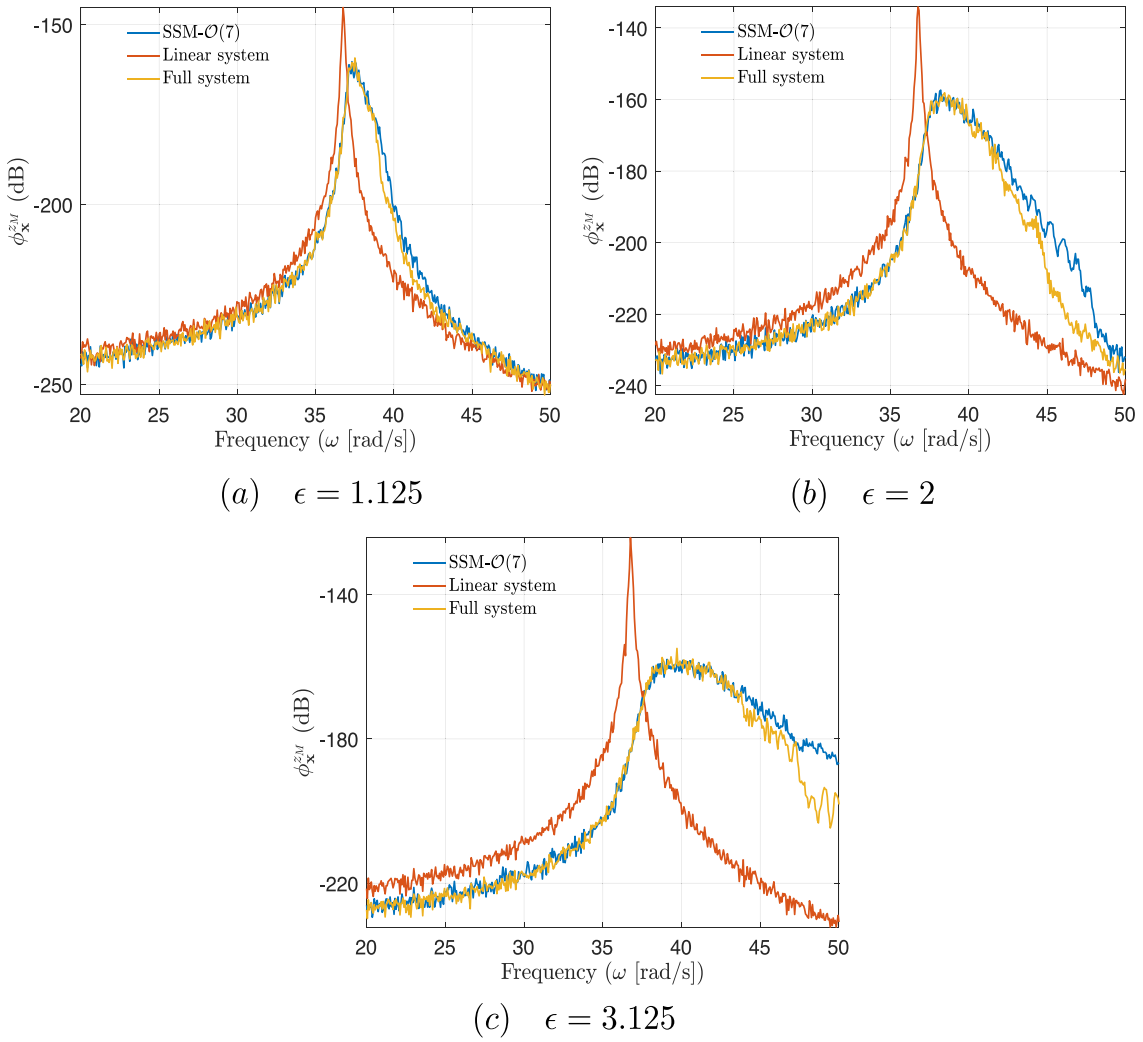

Fig. 10. PSD $\phi_{\mathbf{x}}^{z_M}$ of the out-of-plane displacement of the center point M obtained from the SSM-reduced order model (blue) and from the full-order model (yellow) for two earthquake magnitudes. We also plot in red the numerical PSD for the linear system for different ϵ values. (a) $\epsilon = 1.125$ (small wind pressure fluctuations). (b) $\epsilon = 2$ (moderate wind pressure fluctuations). (c) $\epsilon = 3.125$ (large wind pressure fluctuations). (For interpretation of the references to color in this figure legend, the reader is referred to the web version of this article.)

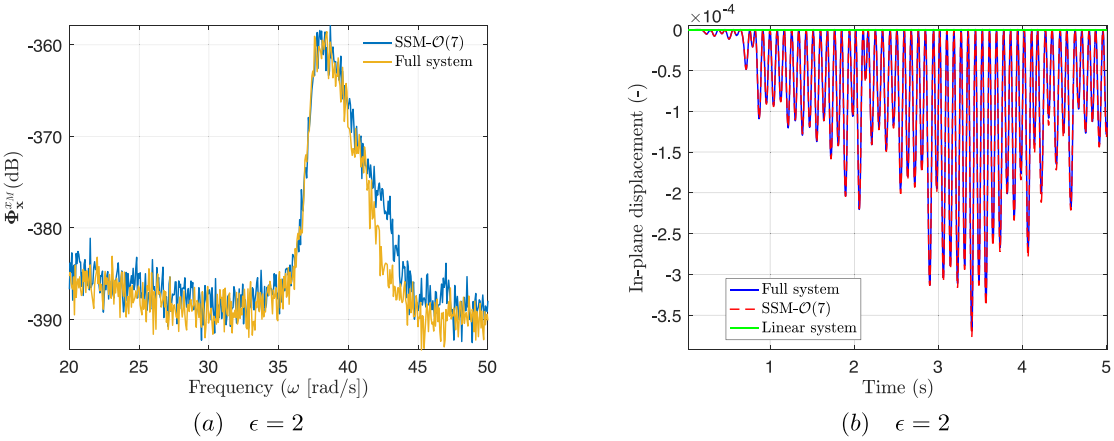

Fig. 11. In-plane displacement of the plate at center point M obtained from the SSM-reduced order model and full order model simulation with moderate forcing $\epsilon = 2$. (a) The PSD $\phi_x^{x_M}$ of the in-plane displacement along x-direction. (b) Time series of the in-plane displacement x_M. The displacement is scaled by the thickness of the plate. (For interpretation of the references to color in this figure legend, the reader is referred to the web version of this article.)

Table 3
Run times for plate model and reduced model for 50 Monte Carlo simulations in the $\epsilon = 3.125$ forcing regime. All computations were performed on MATLAB version 2022b installed on 50 nodes of the ETH Zürich Euler supercomputing cluster with Intel(R) Xeon(R) CPU E3-1284L v4 @ 2.90 GHz processor.

Full system (HH:MM:SS)	2D SSM (HH:MM:SS)	Number of MC simulations
12:50:40	00:01:45	50

In this example, we compute a random SSM-reduced model up to order $N = 7$. We again validate our results with the full order model for $m = 50$ Monte Carlo simulations. In Figs. 10a–c, we see the PSDs of the reduced-order models capture the trends of the true system for increasing forcing magnitudes. These trends are well documented in the literature for plate models (see, e.g., Reinhall and Miles [50]).

In Fig. 11, we also plot the SSM-reduced predictions for the in-plane displacements to compare with the full order model. The SSM-reduced model to accurately predicts these displacements, which solely arise from nonlinear coupling between the in-plane and out-of-plane displacements of the full model of the plate.

The run time comparison between the full and reduced models now yields a dramatic difference. The combined time for constructing the random SSM model and the complete Monte Carlo simulation is under 2 min. For the full order model simulation it takes nearly half a day (13 hours). We refer to Table 3 for the exact solve times.

4. Conclusion

We have extended prior mathematical results on the existence and reduced dynamics of spectral submanifolds (SSMs) from deterministic dynamical systems to dynamical systems with additive and uniformly bounded random noise. While the mathematical proofs of our results are valid for the case of small external random forcing, we expect them to extend to larger forcing values as well, as seen in the examples we presented. This is in line with our findings for moderate deterministic aperiodic forcing (see, e.g., Haller and Kaundinya [17]).

Our main result is that appropriately defined random attracting invariant manifolds perturb from primary attracting SSMs of the deterministic, unforced limit of a dynamical system. These random SSMs are no longer tangent to eigenspaces of the linearized system but continue to be invariant under any given realization of the flow map and have the same degree of smoothness as their unforced counterpart. The leading-order reduced dynamics on the random SSMs consists of the reduced dynamics of the deterministic limit of the SSM with an additive random term. The deterministic SSM-reduced dynamics can be computed via equation-driven or data-driven model reduction applied to the unforced system using SSMTool (Jain et al. [18]) or SSMLearn (see Cenedese et al. [51]), respectively. For state-independent random forcing, the additional random term in the leading-order SSM-reduced dynamics is simply the projection of the random forcing to the spectral subspace.

Trajectories of the full system in the domain of attraction of random SSMs synchronize exponentially fast with trajectories of the SSM-reduced dynamics. This enables us to perform Monte-Carlo simulations directly on the SSM-reduced dynamics to obtain the response statistics of the full system. Such an SSM-reduced computation brings an immense speed-up relative to simulations performed on full finite-element problems. This is generally true for any model obtained from model-reduction tools but SSM-reduction comes with mathematical guarantees and requires no tuning of hyperparameters or training of neural nets. Importantly, the deterministic core of the SSM-reduced dynamics remains the same even if one changes the noise model.

The leading-order SSM-reduction formulas derived in this paper only allow us to test our results with the full order model up to a certain magnitude of forcing. This limitation can be addressed by computing higher-order corrections due to forcing. Such corrections have already been computed in recent work (Haller and Kaundinya [17]) and integration of these results into the package *SSMtool* is currently underway. At this point, those higher-order corrections are already directly applicable to any given realization of a bounded random forcing model, as was illustrated by Haller and Kaundinya [17] for chaotic forcing obtained from numerical simulations of the classic Lorenz attractor.

In this paper, we have illustrated random SSM reduction in an equation-driven setting where the deterministic core of the reduced model was obtained from SSMTool. Data-driven random SSM reduction proceeds along the same lines, with SSMLearn providing the deterministic part of the reduced model. A continually growing body of literature is available on the accuracy of low-dimensional deterministic models obtained from SSMLearn applied to data generated from finite-element models or experimental data, including experimental videos (see Cenedese et al. [21], Cenedese et al. [29], Haller et al. [52], Haller et al. [16], Kaszás et al. [53], Axås and Haller [54], Liu et al. [55], Xu et al. [25], Cenedese et al. [31], Yang et al. [30]). Specific demonstrations of the present results in those data-driven settings will appear elsewhere.

CRediT authorship contribution statement

Zhenwei Xu: Writing – review & editing, Writing – original draft, Visualization, Validation, Software, Investigation. **Roshan S. Kaundinya:** Writing – review & editing, Writing – original draft. **Shobhit Jain:** Writing – review & editing, Supervision, Methodology. **George Haller:** Writing – review & editing, Writing – original draft, Supervision, Methodology, Formal analysis, Conceptualization.

Declaration of competing interest

The authors declare that they have no known competing financial interests or personal relationships that could have appeared to influence the work reported in this paper.

Appendix A. Proof of Theorem 1

Following Li et al. [34], we use the following definition of normal hyperbolicity for random invariant manifolds:

Definition 1. For a fixed $\epsilon \geq 0$, a random invariant manifold $\mathcal{M}(\boldsymbol{\nu})$ of system (1) is *normally hyperbolic* if for almost every $\boldsymbol{\nu} \in \mathcal{V}$ and $x \in \mathcal{M}(\boldsymbol{\nu})$, there exists a splitting

$$T_x X = E^u(x;\boldsymbol{\nu}) \oplus E^c(x;\boldsymbol{\nu}) \oplus E^s(x;\boldsymbol{\nu}), \qquad E^c(x;\boldsymbol{\nu}) = T_x \mathcal{M}(\boldsymbol{\nu}), \qquad x \in \mathcal{M}(\boldsymbol{\nu}),$$

of each tangent space $T_x\mathbb{R}^n$ along $\mathcal{M}(\boldsymbol{\nu})$ into subspaces $E^i(x;\boldsymbol{\nu})$, for $i = u, c, s$, such that

(i) The splitting is C^0 in x and measurable in $\boldsymbol{\nu}$ and has associated projections

$$\Pi^i(x;\boldsymbol{\nu}) : T_x X \to E^i(x,\boldsymbol{\nu}),$$

for $i = u, c, s$, such that

(ii) The splitting is invariant, i.e.,

$$D_x \mathbf{F}_\epsilon^t(x;\boldsymbol{\nu}) E^i(x;\boldsymbol{\nu}) = E^i\left(\boldsymbol{\theta}^t(\boldsymbol{\nu}), \mathbf{F}_\epsilon^t(x;\boldsymbol{\nu})\right), \quad i = u, s.$$

(iii) The splitting is hyperbolic, i.e., there exist $(\boldsymbol{\theta}^t, \mathbf{F}_\epsilon^t)$-invariant random variables $\bar{\alpha}, \bar{\beta} : \mathcal{M} \to (0,\infty)$ with $\bar{\alpha} < \bar{\beta}$ and a tempered random variable $K : \mathcal{M} \to [1,\infty)$ (i.e., $\left|K\left(x;\boldsymbol{\theta}^t(\boldsymbol{\nu})\right)\right|$ has sub-exponential growth as $t \to \pm\infty$ for any $x \in \mathcal{M}(\boldsymbol{\nu})$) such that

$$\left\| D_x \mathbf{F}_\epsilon^t(x;\boldsymbol{\nu}) \Pi^s(x;\boldsymbol{\nu}) \right\| \leq K(x;\boldsymbol{\nu}) e^{-\bar{\beta}(\boldsymbol{\nu},x)t}, \quad t \geq 0,$$
$$\left\| D_x \mathbf{F}_\epsilon^t(x;\boldsymbol{\nu}) \Pi^u(x;\boldsymbol{\nu}) \right\| \leq K(x;\boldsymbol{\nu}) e^{\bar{\beta}(\boldsymbol{\nu},x)t}, \quad t \leq 0,$$
$$\left\| D_x \mathbf{F}_\epsilon^t(x;\boldsymbol{\nu}) \Pi^c(x;\boldsymbol{\nu}) \right\| \leq K(x;\boldsymbol{\nu}) e^{\bar{\alpha}(\boldsymbol{\nu},x)|t|}, \quad t \in \mathbb{R}.$$

The random manifold $\mathcal{M}$ is called *ρ-normally hyperbolic* if $\rho\bar{\alpha} < \bar{\beta}$.

Under our assumptions in Section 2.2, $\mathbf{F}_0^t : X \to X$ is a class C^r deterministic flow map that has a class C^r, ρ-normally hyperbolic, deterministic invariant manifold $\mathcal{W}_0(E)$ with $\rho \leq r$. (In this case, we have $E^u(x;\nu) = \emptyset$, and $\bar{\alpha} = \alpha$ and $\bar{\beta} = \beta$ are deterministic constants in Definition 1.) If $\mathcal{W}_0(E)$ were invariant, then the main result of Li et al. [34] applied to this setting would yield for small enough $\epsilon > 0$ that $\mathbf{F}_\epsilon^t(\cdot;\nu)$ has a unique, class-C^r, compact normally hyperbolic invariant manifold $\tilde{\mathcal{M}}$ that is C^1-close and C^r-diffeomorphic to $\mathcal{W}_0(E)$ for all $\nu \in \mathcal{V}$. Furthermore, $\tilde{\mathcal{M}}$ would be normally attracting. We stress that for a general stochastic differential equations, even small perturbations can lead to large changes in the flow map over short time. For that reason, the related random invariant manifold results of Li et al. [34] would only apply because we assumed uniformly bounded noise.

However, $\mathcal{W}_0(E)$ is not an invariant (boundaryless) manifold but an inflowing-invariant manifold with boundary, as sketched in Fig. 1. While Li et al. [34] also prove related additional results for inflowing-invariant manifolds, those results require the manifold

to be normally repelling. In contrast, $\mathcal{W}_0(E)$ is normally attracting, which makes those additional results Li et al. [34] inapplicable to our setting without further considerations.

The same issue also arises in the classic persistence theory of normally hyperbolic invariant manifolds with boundary, which is only applicable to either normally attracting overflowing-invariant manifolds or normally repelling inflowing-invariant manifolds. This limitation arises from the graph transform method used in proving persistence: the advection of nearby smooth graphs defined over the unperturbed manifolds under the flow map needs to be a contraction mapping in forward or backward time on the space of such graphs. Under such advection, however, candidate graphs over normally attracting *inflowing* invariant manifolds shrink to surfaces that are no longer graphs over their full initial domains; the same is true near normally repelling *overflowing* invariant manifolds in backward time.

To circumvent this issue and still conclude the (nonunique) persistence of the SSM, $\mathcal{W}_0(E)$, of the deterministic part of the random ODE in (1) for $\epsilon > 0$ small enough, we apply the "wormhole" construct of Eldering et al. [35] to extend $\mathcal{W}_0(E)$ smoothly into a $\rho(E)$-normally hyperbolic, class C^r, normally attracting, compact invariant manifold without boundary. Specifically, we invoke Proposition B1 of Eldering et al. [35], which states that any inflowing-invariant, class C^r, normally attracting, ρ-normally hyperbolic invariant manifold $\mathcal{M}_0$ can be extended smoothly so that it becomes a subset of a ρ-normally hyperbolic, normally attracting, class C^r invariant manifold $\hat{\mathcal{M}}_0$ without boundary. In addition, the stable foliation of $W^s(\mathcal{M}_0)$ coincides with that part of the stable foliation of the extended, boundaryless, normally attracting invariant manifold $\hat{\mathcal{M}}_0$. We note that this extension is non-unique and hence any invariant manifold result applied to $\hat{\mathcal{M}}_0$ will unavoidably lose uniqueness when restricted to a statement about $\mathcal{M}_0$.

Applying the above random invariant manifold results of Li et al. [34] to a forward- and backward-invariant manifold extension $\hat{\mathcal{M}}_0$ of $\mathcal{W}_0(E)$, we have Definition 1 satisfied for $\hat{\mathcal{M}}_0$ with $E^u(x;\nu) = \emptyset$, $K(x;\nu) \equiv K_0$, $\tilde{\beta}(\nu, x) \equiv |\mathrm{Re}\,\lambda_{d+1}| - \nu$ and $\tilde{\alpha}(\nu, x) \equiv |\mathrm{Re}\,\lambda_1| - \nu$ for some small $\nu > 0$. The cited results of Li et al. [34] then yield a persisting random invariant manifold $\hat{\mathcal{M}}_\epsilon(\nu)$ that is $\mathcal{O}(\epsilon)$ C^1-close and $C^{\rho(E)}$-diffeomorphic to $\hat{\mathcal{M}}_0$. Passing to a subset $\mathcal{W}_\epsilon(E;\nu)$ of $\hat{\mathcal{M}}_\epsilon(\nu)$ that is a graph over $\mathcal{W}_0(E)$, we finally conclude the (non-unique) persistence of a normally attracting, class $C^{\rho(E)}$ random, inflowing-invariant manifold $\mathcal{W}_\epsilon(E;\theta^t(\nu))$ that is $\mathcal{O}(\epsilon)$ C^1-close and $C^{\rho(E)}$-diffeomorphic to $\mathcal{W}_0(E)$, as claimed in Theorem 1. The $\mathcal{O}(\epsilon)$ C^1-closeness of the forced SSM to the unforced one can actually be improved to $\mathcal{O}(\epsilon)$ $C^{\rho(E)}$-closeness by adding ϵ as a dummy variable to the variables over which the unforced SSM is defined. We finally note that despite the non-uniqueness of the SSM, the Taylor expansion of $\mathcal{W}_\epsilon(E;\theta^t(\nu))$ is unique up to order $C^{\rho(E)}$ in ϵ.

Appendix B. Deriving the leading order random SSM parametrization

We assume the leading-order SSM parametrization $\mathbf{h}_1(\xi;\theta^t(\nu),\epsilon)$ to be C^1 in time. We also make explicit the linear change of coordinates that transforms $\mathbf{A}$ to the block-diagonal structure Eq. (5), given by

$$\begin{aligned}\mathbf{A}_E &= ((\mathbf{V}_E)_L)^{\mathrm{T}}\mathbf{A}(\mathbf{V}_E)_R,\\ \mathbf{B} &= ((\mathbf{V}_F)_L)^{\mathrm{T}}\mathbf{A}(\mathbf{V}_F)_R,\end{aligned} \tag{26}$$

where we have $(\mathbf{V}_E)_R \in \mathbb{R}^{n\times d}$ and $(\mathbf{V}_E)_L \in \mathbb{R}^{n\times d}$ containing column vectors comprising the right and left eigenvectors associated with the slow subspace E. Similarly, $(\mathbf{V}_F)_R \in \mathbb{R}^{n\times(n-d)}$ and $(\mathbf{V}_F)_L \in \mathbb{R}^{n\times(n-d)}$ comprise the right and left eigenvectors associated with the remaining $(n-d)$-dimensional fast subspace F. The linear coordinate change and its inverse between the phase space variable $\mathbf{x}$ and the modal coordinates is

$$\begin{pmatrix}\xi\\ \eta\end{pmatrix} = \begin{bmatrix}((\mathbf{V}_E)_L)^{\mathrm{T}}\\ ((\mathbf{V}_F)_L)^{\mathrm{T}}\end{bmatrix}\mathbf{x}, \qquad \mathbf{x} = \begin{bmatrix}(\mathbf{V}_E)_R & (\mathbf{V}_F)_R\end{bmatrix}\begin{pmatrix}\xi\\ \eta\end{pmatrix}. \tag{27}$$

We also choose orthonormal slow left and right eigenvectors such that $((\mathbf{V}_E)_L)^{\mathrm{T}}(\mathbf{V}_E)_R = \mathbb{I}_d$.

Let us denote the random SSM parametrization in the phase space by

$$\mathbf{x} = \mathbf{w}_\epsilon(\xi;\theta^t(\nu)) = \mathbf{w}_0(\xi) + \epsilon\mathbf{w}_1(\xi;\theta^t(\nu),\epsilon). \tag{28}$$

This is related to the SSM parametrization in modal coordinates as

$$\begin{pmatrix}\xi\\ \mathbf{h}_\epsilon(\xi;\theta^t(\nu))\end{pmatrix} = \begin{bmatrix}((\mathbf{V}_E)_L)^{\mathrm{T}}\\ ((\mathbf{V}_F)_L)^{\mathrm{T}}\end{bmatrix}\mathbf{w}_\epsilon(\xi;\theta^t(\nu)). \tag{29}$$

Differentiating Eq. (28) with respect to time and expressing $\dot{\mathbf{x}}$ from the governing equations, we obtain the invariance equation for the random SSM in the form

$$\begin{aligned}&\left(\mathbf{D}_\xi\mathbf{w}_0(\xi) + \epsilon\mathbf{D}_\xi\mathbf{w}_1(\xi;\theta^t(\nu),\epsilon)\right)\dot{\xi} + \epsilon\dot{\mathbf{w}}_1(\xi;\theta^t(\nu),\epsilon) =\\ &\qquad \mathbf{A}\mathbf{w}_\epsilon(\xi;\theta^t(\nu)) + \mathbf{f}_0\left(\mathbf{w}_\epsilon(\xi;\theta^t(\nu))\right) + \epsilon\mathbf{g}\left(\mathbf{w}_\epsilon(\xi;\theta^t(\nu)),\theta^t(\nu)\right).\end{aligned} \tag{30}$$

Substituting Eq. (12) for $\dot{\xi}$ and collecting terms to $O(\epsilon)$, we obtain the invariance equation at this order as

$$\mathbf{D}_\xi\mathbf{w}_0(\mathbf{0})\mathbf{g}_\xi\left(\mathbf{0},\mathbf{0},\theta^t(\nu)\right) + \dot{\mathbf{w}}_1\left(\mathbf{0};\theta^t(\nu),0\right) = \mathbf{A}\mathbf{w}_1\left(\mathbf{0};\theta^t(\nu),0\right) + \mathbf{g}\left(\mathbf{0},\theta^t(\nu)\right). \tag{31}$$

We choose to calculate the SSM parametrization as a graph over the slow subspace E. The local tangency of the unforced SSM to E at the equilibrium implies $\mathbf{D}_\xi\mathbf{w}_0(\mathbf{0}) = (\mathbf{V}_E)_R$. We also choose the leading-order forcing term for the random reduced ODE (12) to be the projection of the full random forcing onto E, which implies that at $O(\epsilon)$, we have

$$\mathbf{g}_\xi\left(\mathbf{0},\mathbf{0},\theta^t(\nu)\right) = ((\mathbf{V}_E)_L)^{\mathrm{T}}\mathbf{g}\left(\mathbf{0},\theta^t(\nu)\right). \tag{32}$$

These two choices uniquely define the invariance equation satisfied by the leading-order SSM parametrization $\mathbf{w}_1$. Indeed, substituting for these choices in Eq. (31), we arrive at a unique linear inhomogeneous ODE for $\mathbf{w}_1$,

$$\dot{\mathbf{w}}_1\left(\mathbf{0};\boldsymbol{\theta}^t(\boldsymbol{\nu}),0\right)=\mathbf{A}\mathbf{w}_1\left(\mathbf{0};\boldsymbol{\theta}^t(\boldsymbol{\nu}),0\right)+\left(\mathbb{I}_n-(\mathbf{V}_E)_R((\mathbf{V}_E)_L)^{\mathrm{T}}\right)\mathbf{g}\left(\mathbf{0},\boldsymbol{\theta}^t(\boldsymbol{\nu})\right). \tag{33}$$

This equation has the general solution

$$\mathbf{w}_1\left(\mathbf{0};\boldsymbol{\theta}^t(\boldsymbol{\nu}),0\right)=e^{\mathbf{A}(t-t_0)}\mathbf{w}_1\left(\mathbf{0};\boldsymbol{\theta}^{t_0}(\boldsymbol{\nu}),0\right) \tag{34}$$

$$+\int_{t_0}^{t}e^{\mathbf{A}(t-s)}\left(\mathbb{I}_n-(\mathbf{V}_E)_R((\mathbf{V}_E)_L)^{\top}\right)\mathbf{g}\left(\mathbf{0},\boldsymbol{\theta}^s(\boldsymbol{\nu})\right)ds. \tag{35}$$

If we further assume that the spectrum of $\mathbf{A}$ is real negative and the coefficients are uniformly bounded, the limit $t_0\to-\infty$ gives us an unique globally bounded asymptotic expression for $\mathbf{w}_1$,

$$\mathbf{w}_1\left(\mathbf{0};\boldsymbol{\theta}^t(\boldsymbol{\nu}),0\right)=\int_{-\infty}^{t}e^{\mathbf{A}(t-s)}\left(\mathbb{I}_n-(\mathbf{V}_E)_R((\mathbf{V}_E)_L)^{\mathrm{T}}\right)\mathbf{g}\left(\mathbf{0},\boldsymbol{\theta}^s(\boldsymbol{\nu})\right)ds. \tag{36}$$

Here $(\mathbf{V}_E)_R((\mathbf{V}_E)_L)^{\mathrm{T}}$ is the oblique projection operator whose range is the slow subspace E. Expressing this operator as $\mathbf{P}_E$ and using the linear change of coordinates in Eq. (29), we arrive at the final expression for $\mathbf{h}_1(\mathbf{0};\boldsymbol{\theta}^t(\boldsymbol{\nu}),0)$,

$$\mathbf{h}_1(\mathbf{0};\boldsymbol{\theta}^t(\boldsymbol{\nu}),0)=((\mathbf{V}_F)_L)^{\mathrm{T}}\int_{-\infty}^{t}e^{\mathbf{A}(t-s)}\left(\mathbb{I}_n-\mathbf{P}_E\right)\mathbf{g}(\mathbf{0},\boldsymbol{\theta}^s(\boldsymbol{\nu}))ds. \tag{37}$$

Note that Eq. (36) does not require the calculation of the fast eigenvectors and only depends on knowing the slow counterparts. It also directly gives the result in the physical coordinates $\mathbf{x}$, unlike Eq. (15). In practice, we will use Eq. (36) to estimate the leading-order contribution of the random SSM parametrization. We also expect the convolution operation to be dominated by a small finite set of slowly decaying modes outside E when estimating the action of $e^{\mathbf{A}(t-s)}$ on the projected component of the forcing along the fast spectral subspace F.

Since we have chosen a graph-style parametrization for the SSM that projected the external forcing onto the slow dynamics, we expect the complementary projection of the forcing to appear in the SSM parametrization to take into account any shifts in the SSM away from the autonomous equilibrium. Note that $\mathbb{I}_n-\mathbf{P}_E$ is precisely the oblique projection operator that projects the forcing onto the remaining $(n-d)$ fast linear modes. This suggests that if the forcing vector is nearly tangent to the slow subspace E and one is also only interested in predictions for slow observables, we can ignore this leading order contribution as well. In fact, in both data- and equation-driven SSM computations this term is ignored due to these reasons and one is still able to achieve good accuracy in predictions (see Cenedese et al. [21], Axås et al. [22] and Jain and Haller [36]). Also, the smoothness assumption in time for the parametrization is not unreasonable as we can always numerically view continuous random signals as smooth interpolations of the dataset representing them. For all the forcing vectors and forcing magnitudes in our examples (see Section 3), we found the leading-order contribution to be negligible. This indicates that the forcing vectors were nearly tangent to the slow subspace E, in which case one can, in fact, ignore this contribution and still obtain accurate predictions.

Appendix C. Spectral density for linear systems

Consider the randomly forced linear, time-invariant, multi-degree-of-freedom system

$$\mathbf{M}\ddot{\mathbf{q}}+\mathbf{C}\dot{\mathbf{q}}+\mathbf{K}\mathbf{q}=\mathbf{p}(t).$$

By taking the Fourier transform of the above equation, we obtain the energy transfer function in the frequency domain as

$$\mathbf{H}(\omega)=[-\omega^2\mathbf{M}+i\omega\mathbf{C}+\mathbf{K}]^{-1}.$$

If we assume the spectral density matrix of the random forcing $\mathbf{p}(t)$ is $\boldsymbol{\Phi}_{\mathbf{p}}$, we can explicitly calculate the spectral density matrix for $\mathbf{q}$ as

$$\boldsymbol{\Phi}_{\mathbf{q}}(\omega)=\mathbf{H}(\omega)\boldsymbol{\Phi}_{\mathbf{p}}(\omega)\mathbf{H}^{\star}(\omega). \tag{38}$$

When the system is one-dimensional, this relationship simplifies to $\boldsymbol{\Phi}_{\mathbf{q}}(\omega)=\|\mathbf{H}(\omega)\|^2\boldsymbol{\Phi}_{\mathbf{g}}(\omega)$. For the example in Section 3.1, we use the above relation to analytically compute the output response when the system is assumed to be linear. For the example, in Section 3.2, where we apply a reflective boundary for the Itô process, no analytic relationship of the type (38) is available for the linear system, but one can still use this formula as an approximation for the linear response. This also applies to the example in Section 3.3, where we sample from a truncated Gaussian distribution. In this case, although the linear relation is not exact, it serves as a good estimate to capture the overall trend. Lastly, for the example in Section 3.4, not even an approximate analytic relationship is available for the spectrum of the linear response, which prompts us to use Monte Carlo simulations to obtain the linear response.

Data availability

The codes to generate our results are available on the open-source MATLAB software SSMTool.

References

[1] T.K. Caughey, Equivalent linearization techniques, J. Acoust. Soc. Am. 35 (1962) 1706–1711.
[2] S.H. Crandall, Perturbation Techniques for Random Vibration of Nonlinear Systems, J. Acoust. Soc. Am. 35 (11) (1963) 1700–1705.
[3] S.H. Crandall, W.D. Mark, Random Vibration in Mechanical Systems, Academic Press, 2014.
[4] T.K. Caughey, Nonlinear theory of random vibrations, in *Advances in Applied Mechanics*, vol. 11, in: Chia-Shun Yih (Ed.), in: Advances in Applied Mechanics, Elsevier, 1971, pp. 209–253.
[5] P.H. Wirschin, T.L. Paez, K. Ortiz, Random Vibrations: Theory and Practice, Dover, 2006.
[6] J. Li, J. Chen, Stochastic Dynamics of Structures, John Wiley & Sons, 2009.
[7] J.B. Roberts, P.D. Spanos, Stochastic averaging: An approximate method of solving random vibration problems, Int. J. Non-Linear Mech. 21 (2) (1986) 111–134.
[8] L. Arnold, Random Dynamical Systems, Springer-Verlag, Berlin, 2003.
[9] J. Duan, An Introduction to Stochastic Dynamics, Cambridge University Press, city=Cambridge, UK, 2015.
[10] L.E. Ghaoui, G. Calafiore, Bounded uncertainty models in finance: Parameter estimation and forecasting, IFAC Proc. Vol. 35 (1) (2002) 13–18, 15th IFAC World Congress.
[11] S.W. Shaw, C. Pierre, Normal modes for non-linear vibratory systems, J. Sound Vibr. 164 (1) (1993) 85–124.
[12] G. Kerschen, M. Peeters, J.C. Golinval, A.F. Vakakis, Nonlinear normal modes, Part I: A useful framework for the structural dynamicist, Mech. Sys. Signal Proc. 23 (1) (2009) 170–194.
[13] Y.V. Mikhlin, K.V. Avramov, Nonlinears Normal Modes for Vibrating Mechanical Systems. Review of Theoretical Developments, Appl. Mech. Rev, 63 (6) (2011) 060802.
[14] Y. Mikhlin, K.V. Avramov, Nonlinear Normal Modes of Vibrating Mechanical Systems: 10 Years of Progress, Appl. Mech. Rev. (2023) 1–57.
[15] G. Haller, S. Ponsioen, Nonlinear normal modes and spectral submanifolds: existence, uniqueness and use in model reduction, Nonlinear Dyn. 86 (3) (2016) 1493–1534.
[16] G. Haller, B. Kaszás, A. Liu, J. Axås, Nonlinear model reduction to fractional and mixed-mode spectral submanifolds, Chaos 33 (6) (2023) 063138.
[17] G. Haller, R.S. Kaundinya, Nonlinear model reduction to temporally aperiodic spectral submanifolds, Chaos 34 (4) (2024) 043152.
[18] S. Jain, T. Thurner, M. Li, G. Haller, SSMTool 2.3: Computation of invariant manifolds and their reduced dynamics in high-dimensional mechanics problems, 2023, pp. 1417–1450, http://dx.doi.org/10.5281/zenodo.4614201.
[19] T. Thurnher, G. Haller, S. Jain, Nonautonomous spectral submanifolds for model reduction of nonlinear mechanical systems under parametric resonance, Chaos 34 (7) (2024) 073127, http://dx.doi.org/10.1063/5.0168431, _eprint: https://pubs.aip.org/aip/cha/article-pdf/doi/10.1063/5.0168431/20043021/073127_1_5.0168431.pdf.
[20] M. Li, S. Jain, G. Haller, Model reduction for constrained mechanical systems via spectral submanifolds, Nonlinear Dynam. 111 (10) (2023) 8881–8911.
[21] M. Cenedese, J. Axås, B. Bäuerlein, K. Avila, G. Haller, Data-driven modeling and prediction of non-linearizable dynamics via spectral submanifolds, Nature Comm. 13 (2022) 872.
[22] J. Axås, M. Cenedese, G. Haller, Fast data-driven model reduction for nonlinear dynamical systems, Nonlinear Dyn. 111 (2023) 7941–7957.
[23] J.I. Alora, M. Cenedese, E. Schmerling, G. Haller, M. Pavone, Data-driven spectral submanifold reduction for nonlinear optimal control of high-dimensional robots, in: Proc. IEEE Int. Conf. Robotics and Autom. (ICRA), London, 2023, pp. 2627–2633.
[24] B. Kaszás, G. Haller, Capturing the edge of chaos as a spectral submanifold in pipe flows, J. Fluid Mech. 979 (2024) A48.
[25] Z. Xu, B. Kaszás, M. Cenedese, G. Berti, F. Coletti, G. Haller, Data-driven modeling of the regular and chaotic dynamics of an inverted flag from experiments, J. Fluid Mech. (987) (2024) R7.
[26] K. Worden, P.L. Green, A machine learning approach to nonlinear modal analysis, Mech. Syst. Signal Proc. 84 (2017) 34–53.
[27] G. Tsialiamanis, M.D. Champneys, N. Dervilis, D.J. Wagg, K. Worden, On the application of generative adversarial networks for nonlinear modal analysis, Mech. Syst. Signal Proc. 166 (2022) 108473.
[28] T. Simpson, N. Dervilis, E. Chatzi, Machine learning approach to model order reduction of nonlinear systems via autoencoder and LSTM networks, J. Eng. Mech. 147 (10) (2021) 04021061.
[29] M. Cenedese, J. Axås, H. Yang, M. Eriten, G. Haller, Data-driven nonlinear model reduction to spectral submanifolds in mechanical systems, Phil. Trans. R. Soc. A 380 (2022) 20210194.
[30] A. Yang, J. Axås, F. Kádár, G. Stépán, G. Haller, Modeling nonlinear dynamics from videos, Nonlinear Dyn. (2024) http://dx.doi.org/10.1007/s11071-024-10687-8.
[31] M. Cenedese, J. Marconi, G. Haller, S. Jain, Data-assisted non-intrusive model reduction for forced nonlinear finite elements models, Nonlinear Dyn. (2024) http://dx.doi.org/10.1007/s11071-024-10507-z.
[32] X. Cabré, E. Fontich, R. de la Llave, The parameterization method for invariant manifolds I: Manifolds associated to non-resonant subspaces, Indiana Univ. Math. J. 52 (2) (2003) 283–328.
[33] N. Fenichel, Persistence and smoothness of invariant manifolds for flows, Indiana Univ. Math. J. 21 (3) (1971) 193–226.
[34] J. Li, K. Lu, P. Bates, Normally hyperbolic invariant manifolds for random dynamical systems: Part I - Persistence, Trans. AMS 365 (2013) 5933–5966.
[35] J. Eldering, M. Kvalheim, S. Revzen, Global linearization and fiber bundle structure of invariant manifolds, Nonlinearity 31 (2018) 4202–4245.
[36] S. Jain, G. Haller, How to compute invariant manifolds and their reduced dynamics in high-dimensional finite-element models? Nonlin. Dyn. 107 (2022) 1417–1450.
[37] A. Preumont, Random Vibration and Spectral Analysis/Vibrations aléatoires et analyse spectral, vol. 33, Springer Science & Business Media, 2013.
[38] F. Kozin, Autoregressive moving average models of earthquake records, Probab. Eng. Mech. 3 (2) (1988) 58–63.
[39] A. Papoulis, Random variables and stochastic processes, 1965.
[40] M. Geradin, D.J. Rixen, Mechanical Vibrations: Theory and Application to Structural Dynamics, 3rd E., John Wiley & Sons, 2015.
[41] K. Burrage, I. Lenane, G. Lythe, Numerical methods for second-order stochastic differential equations, SIAM J. Sci. Comput. 29 (1) (2007) 245–264.
[42] P.E. Kloeden, E. Platen, Stochastic differential equations, in: Numerical Solution of Stochastic Differential Equations, Springer, 1992, pp. 103–160.
[43] M. Gobbi, G. Mastinu, Analytical description and optimization of the dynamic behaviour of passively suspended road vehicles, J. Sound Vib. 245 (3) (2001) 457–481.
[44] C. Ho, Y. Zhu, Z. Lang, S.A. Billings, M. Kohiyama, S. Wakayama, Nonlinear damping based semi-active building isolation system, J. Sound Vib. 424 (2018) 302–317.
[45] S. Jain, P. Tiso, G. Haller, Exact nonlinear model reduction for a von kármán beam: slow-fast decomposition and spectral submanifolds, J. Sound Vibr. 423 (2018) 195–211.
[46] J.N. Reddy, An Introduction to Nonlinear Finite Element Analysis Second Edition: with Applications to Heat Transfer, Fluid Mechanics, and Solid Mechanics, OUP Oxford, 2014.
[47] S. Jain, J. Marconi, P. Tiso, YetAnotherFECode, 2020, Zenodo https://doi.org/10.5281/zenodo.4011281.
[48] M. Li, S. Jain, G. Haller, Nonlinear analysis of forced mechanical systemswith internal resonance using spectral submanifolds, Part I: Periodic response and forced response curve, Nonlinear Dynam. 110 (2) (2022) 1005–1043.

[49] R. Zárate-Miñano, M. Anghel, F. Milano, Continuous wind speed models based on stochastic differential equations, Appl. Energy 104 (2013) 42–49.
[50] P.G. Reinhall, R.N. Miles, Effect of damping and stiffness on the random vibration of non-linear periodic plates, J. Sound Vib. 132 (1) (1989) 33–42.
[51] M. Cenedese, J. Axås, G. Haller, SSMLearn, 2021, https://github.com/haller-group/SSMLearn.
[52] G. Haller, S. Jain, M. Cenedese, Dynamics-based machine learning for nonlinearizable phenomena: Data-driven reduced models on spectral submanifolds, SIAM News 55 (5) (2022) 1–4.
[53] B. Kaszás, M. Cenedese, G. Haller, Dynamics-based machine learning of transitions in couette flow, Phys. Rev. Fluids 7 (2022) L082402.
[54] J. Axås, G. Haller, Model reduction for nonlinerizable dynamics via delay-embedded spectral submanifolds, Nonlinear Dyn. 111 (2023) 22079–22099.
[55] A. Liu, J. Axås, G. Haller, Data-driven modeling and forecasting of chaotic dynamics on inertial manifolds constructed as spectral submanifolds, Chaos 34 (2024) 033140.